# **Analytical Weak-lensing Shear Responses of Galaxy Properties and Galaxy Detection**

Xiangchong Li 1\*, Rachel Mandelbaum<sup>1</sup>

<sup>1</sup>Department of Physics, McWilliams Center for Cosmology, Carnegie Mellon University, Pittsburgh, PA 15213, USA

Received Month XX, YYYY; accepted Month XX, YYYY

# ABSTRACT

Shear estimation bias from galaxy detection and blending identification is now recognized as an issue for ongoing and future weak-lensing surveys. Currently, the empirical approach to correcting for this bias involves numerically shearing every observed galaxy and rerunning the detection and selection process. In this work, we provide an analytical correction for this bias that is accurate to subpercent level and far simpler to use. With the interpretation that smoothed image pixel values and galaxy properties are projections of the image signal onto a set of basis functions, we analytically derive the linear shear responses of both the pixel values and the galaxy properties (i.e., magnitude, size and shape) using the shear responses of the basis functions. With these derived shear responses, we correct for biases from shear-dependent galaxy detection and galaxy sample selection. With the analytical covariance matrix of measurement errors caused by image noise on pixel values and galaxy properties, we correct for the noise biases in galaxy shape measurement and the detection/selection process to the second-order in noise. The code used for this paper can carry out the detection, selection, and shear measurement for  $\sim 1000$  galaxies per CPU second. The algorithm is tested with realistic image simulations, and we find, after the analytical correction (without relying on external image calibration) for the detection/selection bias of about -4%, the multiplicative shear bias is  $-0.12 \pm 0.10\%$  for isolated galaxies; and about  $-0.3 \pm 0.1\%$  for blended galaxies with Hyper Suprime-Cam observational condition.

**Key words:** gravitational lensing: weak; cosmology: observations; techniques: image processing.

# 1 INTRODUCTION

The observed shape (or shear) distortions of distant galaxy light profiles due to deflection of light by the foreground mass distribution on its path to observers can be used to study the distribution of matter, including both baryonic and dark matter, in the Universe (see Massey et al. 2010; Kilbinger 2015; Mandelbaum 2018 for recent reviews). This deflection of light is known as weak gravitational lensing, which is one of the main science targets of the 'Stage-IV' imaging surveys: the Vera C. Rubin Observatory Legacy Survey of Space and Time<sup>1</sup> (LSST, Ivezić et al. 2019), Euclid<sup>2</sup> (Laureijs et al. 2011), and the Nancy Grace Roman Space Telescope High Latitude Survey<sup>3</sup> (Spergel et al. 2015). These surveys are designed to constrain the fundamental physics of the dark Universe with unprecedented precision with weak lensing. A key challenge in the scientific exploitation of these upcoming datasets is that the noisy images of galaxies have been convolved by the point-spread function (PSF), which modifies the apparent galaxy shapes in a spatially coherent way. To ensure that systematic biases in cosmological weak-lensing analyses are within the statistical uncertainties, these surveys require that the systematic bias in measurement of the shear distortions from the noisy, PSF-convolved galaxy images to be no worse than one part per thousand (Massey et al. 2013; The LSST Dark Energy Science Collaboration et al. 2018).

A few methods developed by the community, namely Metacalibration (see Huff & Mandelbaum 2017; Sheldon & Huff 2017; Sheldon et al. 2020), Bayesian Fourier Domain (BFD, see Bernstein & Armstrong 2014; Bernstein et al. 2016), Fourier Quad (Fourier\_Quad, see Zhang et al. 2017; Li & Zhang 2021) and Fourier power function shapelets (FPFS, see Li et al. 2018, 2022b) are able to reach sub-percent level accuracy for isolated galaxies without relying on calibrations using external image simulation; these methods have other ways to correct for noise bias (Refregier et al. 2012), model bias (Bernstein 2010) and selection bias (Kaiser 2000) in the shear estimation. Sheldon et al. (2020) found that the shear-dependent detection and blending identification causes a few percent-level shear estimation bias. They demonstrated Metadetection to correct for shear biases from source detection by creating counterfactual images with different input shears before detecting sources from pixels. The shear response of the detection process is estimated from the difference in the average of galaxy shapes detected from the counterfactual images. They demonstrated that Metadetection is able to reduce biases from shear-dependent detection below the stage-IV requirements on the control of systematics even for blended galaxies.

In this paper, we analytically derive the correction for sheardependent detection bias at the pixel level based on the framework of the FPFS shear estimator, and we show, with blended galaxy image simulations, that the analytical method reduces the detection-

<sup>\*</sup> xiangchl@andrew.cmu.edu

<sup>1</sup> http://www.lsst.org/

<sup>&</sup>lt;sup>2</sup> Euclid satellite mission: http://sci.esa.int/euclid/

<sup>3</sup> http://roman.gsfc.nasa.gov/

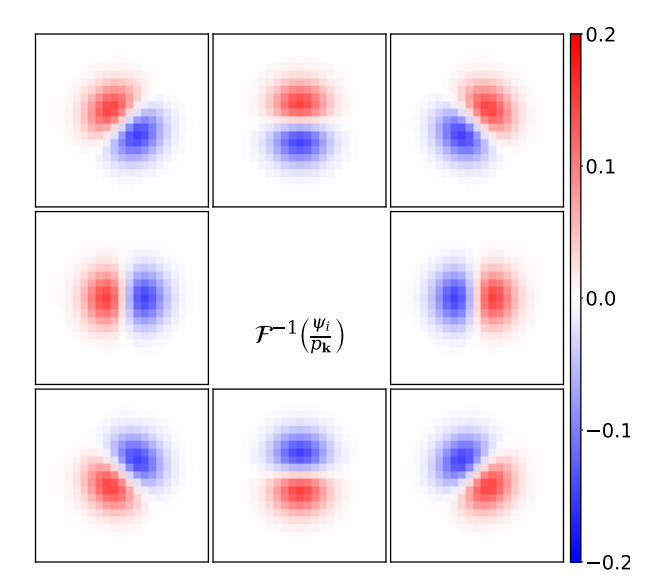


**Figure 1.** Peak basis functions defined in configuration space with respect to postPSF images, which are used to define whether there is a detected peak at the location of each pixel. They are the inverse Fourier transform of  $\psi_i$  deconvolved by the PSF,  $p_k$ , where  $\mathcal{F}^{-1}$  in the figure refers to the inverse Fourier transform operator.

induced shear bias by an order of magnitude, to the sub-percent level. To be more specific, we propose to interpret image pixel values after smoothing as projections of the image field onto a set of basis functions. Based on this new interpretation, we derive the shear responses of the pixel values using the shear responses of the pixel basis functions. Galaxy detection from images is interpreted as a selection using these pixel values, and the selection bias due to the galaxy detection is analytically corrected using the shear responses of the pixel values. Our analytical method is more than 100 times faster than Metadetection, and does not require the generation of multiple catalogs to correct for shear-dependent detection bias.

This paper is organized as follows: In Section 2, we propose an analytical method to correct for shear-dependent detection bias and noise bias at the image pixel level. Then, in Section 3, we introduce the galaxy image simulations that we used to test (not calibrate) the proposed formalism for correcting the above-mentioned shear biases. The results of the tests on isolated and blended galaxies are shown in Section 4. Finally, in Section 5, we summarize our results and the future outlook.

#### 2 METHODOLOGY

In Section 2.1, we introduce the formalism of the FPFS shear estimator, which interprets the lensing shear distortion and image noise as generating perturbations in the galaxy number density in the space of galaxy properties. In Section 2.2, we interpret image pixel values after smoothing as projections onto FPFS pixel basis functions and derive the shear response of smoothed pixel values. In Section 2.3, we define FPFS properties of galaxies to quantify their flux, size and shape; in addition, the shear responses of these quantities are analytically derived. In Section 2.4, we apply the formalism with the FPFS properties and their shear response to correct shear-dependent detection bias and selection bias. In Section 2.5, we derive the co-

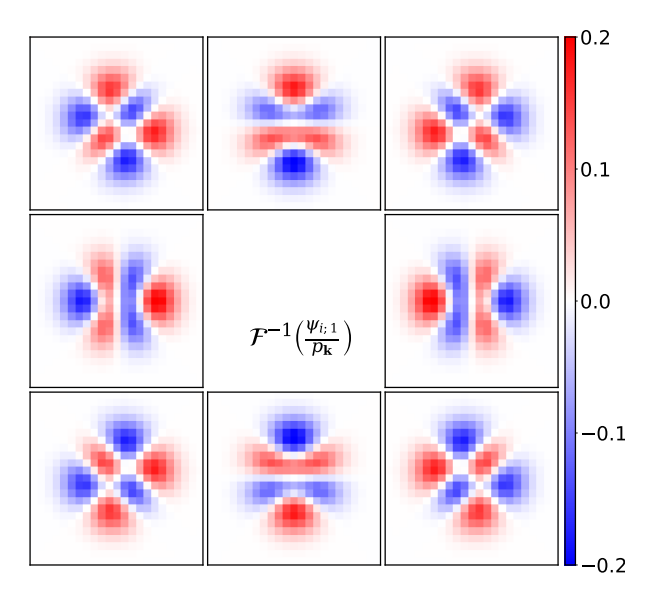


**Figure 2.** The first component shear response of peak basis functions (shown in Figure 1) defined in configuration space with respect to postPSF images, which is the inverse Fourier transform of  $\psi_{i;1}$  deconvolved by the PSF,  $p_k$ .

variance matrix for those introduced FPFS properties. In Section 2.6, we summarize the steps in applying this shear estimator.

# 2.1 Formalism

We first rewrite the works of Li et al. (2018) and Li et al. (2022b) into a general formalism (Sec. 2.1.1). The basic idea is that the statistics of a sample of galaxies can be described by its number distribution in the space of galaxy properties. Within this space, we derive the leading-order perturbations due to weak-lensing shear distortion (Section 2.1.2) and image noise on the galaxy number distribution (Section 2.1.3).

# 2.1.1 Intrinsic noiseless galaxy number distribution

Galaxy ellipticity, which has two components:  $e_{\alpha}$  ( $\alpha \in \{1,2\}$ ), is widely used to infer shear from large samples of galaxies (Bernstein & Jarvis 2002; Hirata & Seljak 2003). It is a spin-2 property of a galaxy, and is normally defined using the second-order moments of galaxy light profiles. In this subsection, we derive corrections for shear-estimation bias within a general framework that can be applied to many different ellipticity definitions. For this reason, we have used  $e_{\alpha}$  without providing a mathematical definition. Once we discuss the specific implementation of this formalism used in this paper, we will provide our ellipticity definition used for shear estimation (Section 2.3).

For a galaxy sample with normalized probability density function (PDF; denoted as  $\mathcal{P}$ ) in galaxy property space, the expected average of the weighted galaxy ellipticities is

$$\langle we_{\alpha} \rangle = \int de_{\alpha} dw \mathcal{P}(e_{\alpha}, w) e_{\alpha} w,$$
 (1)

where  $e_{\alpha}$  and w are galaxy ellipticity and selection weight, respectively. Here the selection weight is a non-negative spin-0 function of galaxy properties, and a galaxy is removed from the sample if

the selection weight equals zero. We propose to estimate the shape and selection weight for each smoothed image pixel and then select a subset of them as galaxy candidates using the selection weights. Following this line of thought, the galaxy detection from pixels is interpreted as applying hard-thresholding weights to the pixels. Also, the selection of a galaxy sub-sample is interpreted as applying hardthresholding weights to the galaxy candidates. The origin of detection and selection bias is that the weights have a nonzero response to weak-lensing shear. Note, this selection weight is different from the traditional shape weight for optimal galaxy shape estimation (see e.g., Mandelbaum et al. 2018b), and we choose not to normalize the average of weighted ellipticity by the average of the selection weight to avoid introducing another shear response from the average selection weight into the shear estimator. The ellipticity and selection weight are multivariable functions of a set of basis modes,  $\mathbf{v} = (v_0, v_1, \dots)$ , where each element,  $v_i$ , is a linear projection of the image onto a basis function (e.g., a Gaussian function centered at a specific pixel). We can write the integral in equation (1) as a summation over  $N_{\rm gal}$  galaxies indexed by l, since the number of galaxies is finite in reality:

$$\langle we_{\alpha} \rangle = \frac{1}{N_{\rm val}} \sum_{l=1}^{N_{\rm gal}} w^{(l)} e_{\alpha}^{(l)} \,. \tag{2}$$

Again, this is an average of weighted ellipticity, not the weighted average of ellipticity, since the denominator in equation (2) is fixed to  $N_{\rm gal}$  rather than the summation over the weights. Note,  $N_{\rm gal}$  refers to the total number of galaxies in the Universe, which is not changed by the lensing distortion. Although  $N_{\rm gal}$  is unmeasurable, as will be shown in our shear estimator (equation (5)), the  $N_{\rm gal}$  normalization for the nominator and the denominator cancel with each other, so that we do not need to know  $N_{\rm val}$  for shear estimation.

The first assumption (assumption 1) in shear estimation is that intrinsic (unlensed) galaxies are randomly oriented; as a result, the expectation values of non-spin-0 properties of intrinsic galaxy light profiles are zero due to rotation symmetry (see Appendix B for details). Ellipticity is a spin-2 property; therefore, the average ellipticity of intrinsic galaxy light profiles equals zero. In addition, given that the selection weight does not include any spin-2 component, the average of the intrinsic (unlensed) weighted ellipticity equals zero.

However, due to weak-lensing shear distortion on galaxies, which is caused by a foreground inhomogeneous mass distribution, the average of the (weighted) ellipticity of observed galaxy light profiles deviates from zero. Here

$$A = \begin{pmatrix} 1 - \gamma_1 & -\gamma_2 \\ -\gamma_2 & 1 + \gamma_1 \end{pmatrix} \tag{3}$$

is the Jacobian matrix of the mapping from the lensed sky to the true sky. The quantities  $(\gamma_1, \gamma_2)$  represent the shear distortion:  $\gamma_1$  stretches the image in the horizontal direction of the sky coordinate system, and  $\gamma_2$  stretches the image in the direction at an angle of 45 deg with the horizontal direction. Note that we set the convergence from lensing distortion (Bartelmann & Schneider 2001) to zero to simplify the notation. We denote the intrinsic ellipticity and intrinsic selection weight as  $\bar{e}_{\alpha}$  and  $\bar{w}$ , respectively. Symbols with bars are for intrinsic (unlensed) properties. A summary of our notation, and how we indicate intrinsic, lensed, and other types of properties, are summarized in Table 1, which is the same as Table 1 of Li et al. (2022b).

In addition to the shear distortion, image noise (which includes read noise, and photon noise from background and sources) also changes the average ellipticity. The second assumption (assumption 2) in shear estimation is that the PDF of image noise is

**Table 1.** Table for accent notations. The examples are for the ellipticity, but the notation also applies to other quantities.

Accented ellipticity	Definition
$\bar{e}_{1,2}$	intrinsic (unlensed) galaxy ellipticity
$e_{1,2}$	ellipticity of lensed galaxies
$ ilde{e}_{1,2}$	ellipticity of noisy lensed galaxies
$\widehat{e}_{1,2}$	ellipticity after noise bias correction

symmetric with respect to zero; as a result, for a basis mode defined with a linear operation on the image, the PDF of the measurement error of the basis mode,  $\delta v_i$ , is symmetric with respect to zero, and the expectation values of any odd-order statistics of the measurement error are also zero. Although a Poisson distribution is not symmetric about its mean, in the background dominated regime, the asymmetry can be neglected and the assumption holds true. The covariance (second-order statistics) between two different modes with index i and j is denoted as  $K_{v_i}^{v_j} = \langle \delta v_i \delta v_j \rangle$ . It is worth mentioning that one can also define basis modes as a linear operation on the power of the image after subtracting the expectation value of the power of the image noise (Zhang et al. 2015; Li & Zhang 2016).

The lensed images are convolved with the PSF, and galaxy shapes are changed by the PSF. As a result, the PSF changes the distribution in the galaxy number density space,  $\mathcal{P}(e_{\alpha}, w)$ . However, we measure the basis modes  $v_i$  from galaxies after deconvolving the PSF in Fourier space (Zhang 2008; Li et al. 2018) – so the influence of the PSF is removed by the deconvolution, assuming that the PSF is accurately determined.

#### 2.1.2 Shear perturbation

The average of the weighted ellipticity transforms under the shear distortion as

$$\langle we_{\alpha} \rangle = \langle \bar{w}\bar{e}_{\alpha} \rangle + \sum_{\beta=1,2} \frac{\partial \langle we_{\alpha} \rangle}{\partial \gamma_{\beta}} \gamma_{\beta} + O\left(\gamma^{3}\right). \tag{4}$$

Assuming that the selection weight, w, is a spin-0 scalar, the average of the intrinsic weighted ellipticity,  $\langle \bar{w}\bar{e}_{\alpha}\rangle$ , is identically zero (assumption 1). Since the shear distortion satisfies  $\gamma_{\alpha} \ll 1$ , the leading order in equation (4) is the first order in shear, which is a vector perturbation in the galaxy number space. The off-diagonal terms in the 2 × 2 shear response matrix,  $\frac{\partial (we_{\alpha})}{\partial \gamma_{\beta}}$  ( $\alpha \neq \beta$ ), are spin-4 properties of intrinsic galaxy light profiles, the expectation values of which are identically zero (assumption 1). The term with the second order in shear is also identically zero due to the rotation symmetry. We find that, in the weak-lensing regime with typical amplitude of shear  $\sim 0.03$ , the neglected third-order term is about  $0.03^3$  (the corresponding bias is  $< 1 \times 10^{-3}$  relative to the shear), which is less than the requirement for the stage-IV weak-lensing survey and hence negligible. We refer the reader to Appendix A for detailed discussions of the second-order and thid-order shear perturbations. In addition, we summarize the spin number of galaxy properties and review their rotation symmetries in Appendix B.

According to Huff & Mandelbaum (2017), the shear response of the average of weighted ellipticity is the first-order derivative of the average of weighted ellipticity to the shear distortion, and the shear

can be estimated by

$$\widehat{\gamma}_{\alpha} = \frac{\langle w e_{\alpha} \rangle}{\mathcal{R}_{\alpha}} \,, \tag{5}$$

where  $\mathcal{R}_{\alpha} \equiv \frac{\partial \langle we_{\alpha} \rangle}{\partial \gamma_{\alpha}}$  are the shear responses (the diagonal terms) of the average of the weighted ellipticity<sup>4</sup>. From the rotational symmetry arguments,  $\mathcal{R}_1$  and  $\mathcal{R}_2$  are expected to be identical; however, we treat them independently in the analysis as a sanity check.

We substitute equation (2) into the definition of  $\mathcal{R}_{\alpha}$  and apply the derivative chain rule to write the shear response in terms of our basis modes  $v_i$  as

$$\mathcal{R}_{\alpha} = \langle w e_{\alpha;\alpha} + w_{;\alpha} e_{\alpha} \rangle 
= \frac{1}{N_{\text{gal}}} \sum_{l=1}^{N_{\text{gal}}} \sum_{i} \left( w^{(l)} \frac{\partial e_{\alpha}^{(l)}}{\partial v_{i}} v_{i;\alpha}^{(l)} + e_{\alpha}^{(l)} \frac{\partial w^{(l)}}{\partial v_{i}} v_{i;\alpha}^{(l)} \right),$$
(6)

where the subscript ';  $\alpha$ ' refers to the partial derivative with respect to one component of shear,  $\gamma_{\alpha}$ . Similar to the weighted ellipticity, we can apply the derivative chain rule to get the first-order (leading-order) shear response for other weighted observables.

One can follow the approach of Metacalleration to obtain the shear responses of the observables (e.g.,  $v_{i;\alpha}$ ,  $e_{\alpha;\alpha}$ ) in real observations by creating counterfactual images with different input shears and measuring the difference in the observables for different shears. This is a finite-difference construction of a shear response as a derivative. In this paper, we take a different approach, consistent with that of Li et al. (2018): we use the shear response of a set of basis functions (in other words, basis coordinates), e.g., shapelets (Refregier 2003; Bernstein & Jarvis 2002), to derive the shear response of any observables constructed with these basis functions. This approach of analytically calculating the impact of shear on the coordinate system (basis functions) avoids repeatedly shearing each galaxy to derive shear responses; therefore, it saves significant computational time.

#### 2.1.3 Noise perturbations

Generally speaking, the weighted ellipticity,  $we_{\alpha}$ , and its shear response are nonlinear functions<sup>5</sup> of  $v_i$ . As a result of this non-linearity, image noise biases the measurement of these nonlinear observables (Refregier et al. 2012). As shown in Sheldon & Huff (2017), such a noise bias can be statistically corrected by adding artificially sheared noise fields with the same statistical properties but different realizations to the observed images. We take the alternate approach proposed by Li et al. (2022b), Taylor expanding the noisy observables as functions of  $\delta v$  and analytically deriving the leading order noise bias correction using the covariance of the measurement error, which can be determined from the images.

To be more specific, we take the expectation value of the noisy weighted ellipticity, denoted as  $\langle \tilde{w}\tilde{e}_{\alpha} \rangle$  (noisy observables are denoted with tilde), as an example:

$$\langle \tilde{w}\tilde{e}_{\alpha} \rangle = \langle we_{\alpha} \rangle + \frac{1}{2} \sum_{i,j} \left( \frac{\partial^{2}(\tilde{w}\tilde{e}_{\alpha})}{\partial v_{i}\partial v_{j}} \delta v_{i} \delta v_{j} \right) + O\left( (\delta v_{i})^{4} \right), \tag{7}$$

where  $\frac{\partial^2(\bar{w}\bar{e}_a)}{\partial v_i \partial v_j}$  is the Hessian matrix of the weighted ellipticity with respect to the basis modes. The odd-order terms (e.g., the first- and third-order terms) of the measurement error reduce to zero after averaging over a large number of galaxies (**assumption 2**). Li et al.

(2018) constructed a weighted ellipticity using shapelets mode to ensure that

$$\left| \frac{\partial^{(n+1)}(we_{\alpha})}{(\partial v_i)^{(n+1)}} (\delta v_i)^{(n+1)} \right| \ll \left| \frac{\partial^n (we_{\alpha})}{(\partial v_i)^n} (\delta v_i)^n \right|, \tag{8}$$

so that the second-order term of the noise residual, which is a tensor perturbation in the space of galaxy properties, is the dominant term beyond  $\langle we_{\alpha} \rangle$  in equation (7), and higher even-order terms can be neglected.

We introduce the debiased weighted ellipticity,  $\widehat{we_a}$ , following Li et al. (2022b). Its expectation value is

$$\langle \widehat{we_{\alpha}} \rangle \equiv \langle \widetilde{w}\widetilde{e}_{\alpha} \rangle - \frac{1}{2} \sum_{i,j} \left\langle \frac{\partial^{2}(\widetilde{w}\widetilde{e}_{\alpha})}{\partial v_{i} \partial v_{j}} K_{v_{j}}^{v_{i}} \right\rangle. \tag{9}$$

The correction term is proportional to the expectation value of the contraction between the Hessian matrix of the nonlinear observable:  $\frac{\partial^2 (\bar{w}\bar{e}_\sigma)}{\partial v_i \partial v_j} \text{ and the noise covariance matrix of linear variables } v_i \text{ and } v_j \text{:} \\ K_{v_j}^{v_i} = \langle \delta v_i \delta v_j \rangle \text{. We investigate the Hessian matrix in detail in Appendix C by separating its elements into zeroth-, first- and higher-order derivatives in the selection weight. The covariance matrix of these linear observables is derived for homogeneous noise in Section 2.5 using the correlation function of noise between pixels. It worth mentioning that in Li et al. (prep) we use auto-differentiation in jax <sup>6</sup> to automatically derive the shear response and second-order noise bias correction following equations (6) and (9).$ 

Similar to the weighted ellipticity, we can derive the second-order (i.e., leading-order) noise bias correction for the expectation value of its shear response (see Appendix C for details). We denote the debiased shear response as  $\widehat{\mathcal{R}}_{\alpha}$ , and the shear estimator is

$$\widehat{\gamma}_{\alpha} = \frac{\langle \widehat{we_{\alpha}} \rangle}{\widehat{\mathcal{R}}} \,. \tag{10}$$

In the following context, we will compress images into a basis vector space of  $(v_0, v_1, ...)$ , which meets the following requirements:

- (i) For each element,  $v_i$ , its shear response,  $\partial v_i/\partial \gamma_\alpha$ , can be analytically derived and measured from images;
- (ii) The covariance matrix of measurement errors,  $K_{v_i}^{v_j}$ , can be analytically derived and measured from images.

With these basis modes, we can derive the shear response of the average weighted ellipticity and correct the noise bias.

# 2.2 Shear response of re-smoothed pixels

In order to derive the shear response of the detection process, we reinterpret the re-smoothed pixel values as projections of the image signal onto a set of pixel basis functions in Section 2.2.1. Benefiting from this interpretation, we derive the linear shear response of the smoothed pixels in Section 2.2.2. Based on the pixel basis functions and their shear response, we define a set of peak basis functions to determine whether there is a detected peak at the location of each pixel and derive the shear response of these peak basis functions in Section 2.2.3. The peak modes and their responses will be used to define detection and selection, and to correct for shear-dependent biases in these processes in Section 2.4.

<sup>&</sup>lt;sup>4</sup> Metadetection (Sheldon et al. 2020) retains the off-diagonal spin-4 terms.

<sup>&</sup>lt;sup>5</sup> Some shear estimators (see, e.g. Zhang et al. 2017) avoid using any non-linear observables.

<sup>6</sup> https://github.com/google/jax

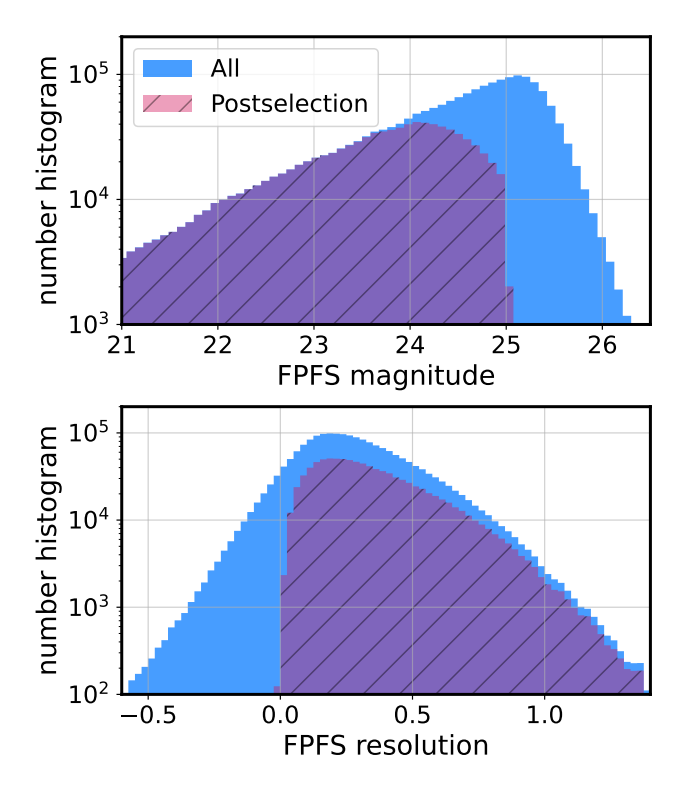


**Figure 3.** Number histograms as functions of FPFS magnitude ( $m_{\rm F}$ , upper panel) and FPFS resolution ( $R_2$ , lower panel) measured from isolated noisy galaxies with HSC-like noise, pixel size and PSF seeing. The unhatched histograms are for all of the galaxies in the isolated simulation described in Section 3; hatched histograms are after the selection with soft cuts (Section 2.4) at  $m_{\rm F}=25$  and  $R_2=0.05$  to select galaxies that are sufficient for weak-lensing science.

#### 2.2.1 Pixel basis functions

The observed astronomical images are smoothed by the PSF from the atmosphere and the telescope optics. We focus on well-sampled images, so that one can transform the pixelated images into a continuous image signal without loss of information according to the Shannon sampling theorem.

The intrinsic image signal (prelensing, prePSF) at a position x in configuration space is denoted as  $\bar{f}_x$ , the lensed image signal distorted by shear  $\gamma$  is denoted as  $f_x$ , and the observed image signal smeared by a PSF,  $p_k$ , is denoted as  $f_x^p$ . Note that in this paper,  $f_x \equiv f(x)$  and  $f_k \equiv f(k)$  are used to denote the signal in configuration space and Fourier space, respectively.

Here we define basis modes for the pixels of re-smoothed images, neglecting the shear distortion. The transformation of the pixel values under a shear distortion will be studied in Section 2.2.2.

An image signal,  $f_x$ , can be transformed into Fourier space and the Fourier transform at wave number k is

$$f_k = \iint \mathrm{d}^2 x \, f_x e^{-\mathrm{i}k \cdot x} \,, \tag{11}$$

where  $i^2 = -1$  is used to denote the complex number symbol to distinguish it from the indexing symbol, *i*.

We re-smooth the observed image, which is originally smoothed by the PSF, with a smoothing kernel to transform the PSF to an isotropic Gaussian. The re-smoothing kernel is defined in Fourier space as multiplication by  $h_k/p_k$ , which is an isotropic Gaussian kernel, denoted as  $h_k = \exp(-|\mathbf{k}|^2 \sigma_h^2/2)$ , deconvolved by the PSF of

the observed image,  $p_k$ .  $\sigma_h$  is the scale radius of the Gaussian kernel in configuration space. Note, the typical scale radius of the target Gaussian kernel should be greater than the typical scale radius of the original PSF in configuration space so that the convolution does not amplify the noise on small scales (large |k|). This re-smoothed image is denoted as  $f_x^h$ , where the superscript indicates that it is the prePSF signal convolved with Gaussian,  $h_x$ .

We will detect peaks from the re-smoothed image as galaxy candidates and measure shear from the detected galaxy sample. In order to correct the shear estimation bias caused by shear-dependent detection at the pixel level, we need to derive the shear response of each pixel on the re-smoothed image. We reinterpret the pixel values of the re-smoothed image as a projection of the continuous image signal onto a *pixel basis function*; here we define this interpretation, and the lensing shear distortion is taken into account in Section 2.2.2. The re-convolved image signal in configuration space is the inverse Fourier transform of  $f_k^*$ :

$$f_x^h = \frac{1}{(2\pi)^2} \iint d^2k \ f_k^h e^{ik \cdot x} = \frac{1}{(2\pi)^2} \iint d^2k \ f_k h_k e^{ik \cdot x} \,. \tag{12}$$

We focus on one specific pixel located at position  $x^0$ . The value of the image at the location of this pixel is

$$f_{x^0}^h = \iint d^2k \ f_k \left\{ \frac{1}{(2\pi)^2} e^{-|k|^2 \sigma_h^2/2} e^{ik \cdot x^0} \right\} . \tag{13}$$

By interpreting the term in the bracket as the *basis function* for the pixel at  $x^0$ :

$$\phi_{x^0}^*(\mathbf{k}) = \frac{1}{(2\pi)^2} e^{-|\mathbf{k}|^2 \sigma_h^2/2} e^{i\mathbf{k} \cdot \mathbf{x}^0} , \qquad (14)$$

we redefine the pixel value as a projection of the image signal in Fourier space onto the pixel basis function:

$$f_{x^0}^h = \iint d^2k \ \phi_{x^0}^*(k) f_k \ . \tag{15}$$

With this interpretation, we can derive the shear response of a pixel value using the shear response of its pixel basis function.

#### 2.2.2 Shear response of re-smoothed pixels

We study the influence of the weak-lensing shear distortion on the re-smoothed pixel values. In configuration space, shear distorts the local coordinate system:  $x = A^{-1}\bar{x}$ , and it conserves surface brightness density:  $f_x = \bar{f}_{\bar{x}}$ . With the assumption that the convergence  $\kappa = 0$ , we have  $k = A\bar{k}$  and  $f_k = \bar{f}_{\bar{k}}$ . Here  $\bar{x}$  and  $\bar{k}$  refer to the coordinates before shear distortion in configuration space and Fourier space, respectively.

Following our new interpretation introduced in Section 2.2.1, the pixel value of the distorted signal is a projection of the distorted signal onto the pixel basis function defined on the distorted coordinates:

$$f_{x^0}^h = \iint d^2k \; \phi_{x^0}^*(\mathbf{k}) \, f_{\mathbf{k}} = \iint d^2\bar{k} \; \phi_{x^0}^*(\mathbf{A}\bar{\mathbf{k}}) \, \bar{f}_{\bar{\mathbf{k}}} \,. \tag{16}$$

This equation suggests that we can determine how the smoothed pixel value,  $f_{x^0}^h$ , transforms by studying how the pixel basis function,  $\phi_{x^0}(Ak)$ , transforms under a shear distortion, keeping the cut value fixed.

Since the lensing shear distortion is small in the weak-lensing regime, we Taylor expand the basis as a function of  $\gamma_{1,2}$  and only keep the first order of  $\gamma_{1,2}$ :

$$\phi_{\mathbf{x}^0}(A\mathbf{k}) = (1 + \gamma_1 S_1 + \gamma_2 S_2) \phi_{\mathbf{x}^0}(\mathbf{k}), \tag{17}$$

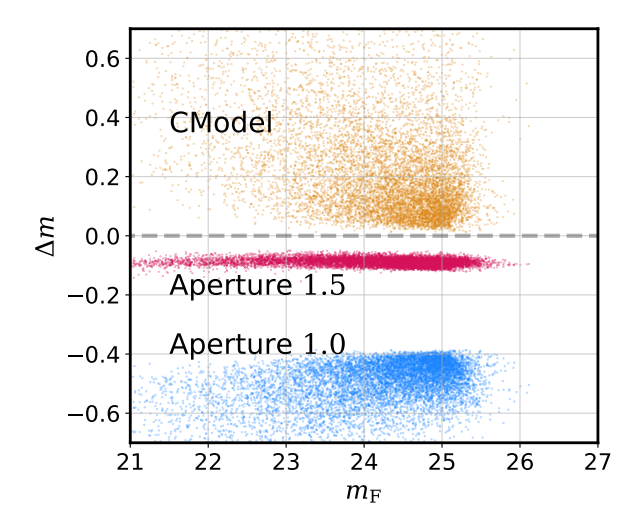


**Figure 4.** Scatter plot of the difference between FPFS magnitude and other magnitude measurements,  $m_{\text{other}}$ , versus FPFS magnitude,  $m_{\text{F}}$ .  $\Delta m = m_{\text{F}} - m_{\text{other}}$ , where  $m_{\text{other}}$  is measured by the HSC pipeline (Bosch et al. 2018). The three magnitude measurements from the HSC pipeline include aperture fluxes with diameter 1".0 (lower) and 1".5 (middle), and CModel (upper) fluxes. The horizontal dashed line is for  $\Delta m = 0$ . As shown in the figure, the 1".5 galaxy aperture flux has the least scatter and the smallest offset with respect to the FPFS magnitude since the effective smoothing scale of the FPFS galaxy flux is very close to the aperture with diameter 1".5.

where  $S_{1,2}$  are the two components of the linear shear distortion operator in Fourier space. Based on the derivative chain rule, we have:

$$S_1 = -\left(k_1 \frac{\partial}{\partial k_1} - k_2 \frac{\partial}{\partial k_2}\right), \qquad S_2 = -\left(k_1 \frac{\partial}{\partial k_2} + k_2 \frac{\partial}{\partial k_1}\right).$$
 (18)

By substituting equation (18) into equation (17), we find that the responses of the pixel basis to the two components of shear distortion,  $(\gamma_1, \gamma_2)$ , are

$$\phi_{x^{0};1} \equiv \frac{\partial \phi_{x^{0}}}{\partial \gamma_{1}} = \left( (k_{1}^{2} - k_{2}^{2}) \sigma_{h}^{2} + i x_{1}^{0} k_{1} - i x_{2}^{0} k_{2} \right) \phi_{x^{0}}, 
\phi_{x^{0};2} \equiv \frac{\partial \phi_{x^{0}}}{\partial \gamma_{2}} = \left( (2 k_{1} k_{2}) \sigma_{h}^{2} + i x_{2}^{0} k_{1} + i x_{1}^{0} k_{2} \right) \phi_{x^{0}}.$$
(19)

Using equations (16) and (19), we derive the responses of the pixel value to the two components ( $\alpha = 1, 2$ ) of shear distortion

$$f_{x^0;\alpha}^h \equiv \frac{\partial f_{x^0}^h}{\partial \gamma_\alpha} = \iint \mathrm{d}^2 k \; \phi_{x^0;\alpha}^* f_k \,. \tag{20}$$

## 2.2.3 Peak detection from images

We propose to use eight basis modes for each pixel in order to characterize the pixel value with respect to other nearby pixels, and thereby identify peaks which could serve as galaxy candidates. We refer to these as 'peak modes'. Taking a pixel centered at  $x^0$  as an example, we define the peak modes of this pixel as

$$q_i = f_{x^0}^h - f_{x^0 + (\cos(i\pi/4), \sin(i\pi/4))}^h, \tag{21}$$

where  $i \in \{0, 1, ..., 7\}$ , and  $(\cos(i\pi/4), \sin(i\pi/4))$  are shifting vectors in the image plane with length equals one.

The shifting vectors have eight different directions separated by  $\pi/4$  to ensure that the peak detection based on these peak modes does not induce any non-zero spin-2 or spin-4 anisotropy. The modes with

shifting vectors along the horizontal and vertical directions are the values of the four adjacent pixels. If we only use these four modes to do galaxy detection, there is a spin-4 leakage in the shear estimation. This leakage would have three consequences: (1) the average amplitudes of the two components of intrinsic ellipticity would differ:  $\langle \bar{e}_1^2 \rangle \neq \langle \bar{e}_2^2 \rangle$ ; (2) the expectation values of the off-diagonal terms of the shear response matrix,  $\langle e_{1;2} \rangle$  and  $\langle e_{2;1} \rangle$ , would be nonzero; and (3) the expectation values of the diagonal terms of the response matrix would not be identical. If this spin-4 leakage is not treated correctly (e.g., using the average between  $\mathcal{R}_1$  and  $\mathcal{R}_2$  for shear estimation), it would cause a shear-estimation bias close to 1%. Therefore, we use eight basis modes instead of four.

The corresponding peak basis functions for the peak modes are

$$\psi_i = \phi_{x^0} - \phi_{x^0 + (\cos(i\pi/4), \sin(i\pi/4))}, \qquad (22)$$

and the shear responses of these peak basis functions are combinations of the pixel response functions,  $\phi_{x:a}$  defined in equation (19):

$$\psi_{i;\alpha} = \phi_{x^0;\alpha} - \phi_{x^0+(\cos(i\pi/4),\sin(i\pi/4));\alpha}, \qquad (23)$$

where  $\alpha \in \{1,2\}$ . The shear responses of the peak modes,  $q_{i;\alpha}$ , can be measured by projecting the prePSF galaxy image signal onto the shear response functions:

$$q_{i;\alpha} = \iint d^2k \,\psi_{i;\alpha} \, f_k \,. \tag{24}$$

We will discuss in detail how to correct the bias from sheardependent detection using the shear response of the peak modes in Section 2.4.

The definitions of peak basis functions and their shear responses are given in Fourier space with respect to images deconvolved from the PSF (prePSF images). Since the operations of the PSF deconvolution and the projections onto the basis functions are commutative and associative, we can combine the PSF deconvolution with the projection operator, and the combined peak basis functions and their shear responses are  $\psi_i/p_k$  and  $\psi_{i;1}/p_k$ . The peak modes and their shear responses can also be estimated by directly projecting PSF-convolved (postPSF) images onto the combined bases that are defined with respect to the postPSF images. In Figures 1 and 2, we show the combined basis functions in configuration space, which are the inverse Fourier transforms of  $\psi_i/p_k$  and  $\psi_{i;1}/p_k$ .

We identify local peaks as potential galaxies by adding a selection weight on the peak modes, and use the corresponding shear responses of the peak modes to correct the bias from shear-dependent detection, which will be covered in Section 2.4.

In real observations, the PSF is spatially varying on an image. To mitigate the influence of PSF variations, we first convolve the image with the re-smoothing kernel, and conduct a preselection to find candidates of local peaks from the re-smoothed images with *loose* selections on peak modes and re-smoothed pixel vales. After the pre-selection, we conduct a postselection by measuring peak modes and the galaxy properties that will be introduced in Section 2.3 for each peak candidate and applying *strict* cuts on them to select galaxies. For the convolution in the preselection, we use the average PSF of the image to define the re-smoothing kernel; whereas in the postselection, we use the PSF model for each peak candidates. If the strict cuts from the postselection select a conservative subset of the initial peak candidates, the PSF variation in real observations does not lead to a bias in the peak identification.

We note that for our detection algorithm, a galaxy that is close to a pixel edge or corner can be "detected" 2 or 4 times, respectively, but with weights approximately 0.5 or 0.25 each time. In addition, the

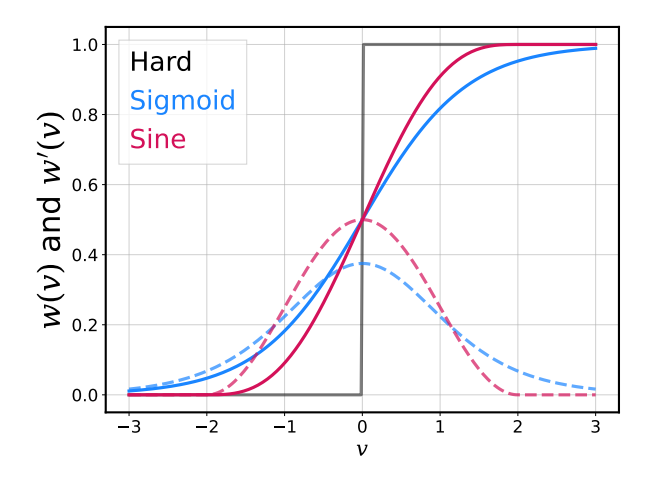


**Figure 5.** Selection functions (solid lines) and their first-order derivative (dashed lines) of hard, sigmoid (equation (45)) and truncated sine (equation (46)) cuts. The smoothness parameter is set to  $\omega = 2$ . We do not show the first-order derivative of the hard cut since that goes to infinity at v = 0.

measurement center for every detection is at the center of the corresponding peak pixel, and refining the estimated galaxy centroid is not possible since we cannot analytically compute the shear response of centroid refinement. In future works, we will further optimize these aspects of our detection algorithm.

# 2.3 Shear response of galaxy properties

In addition to the peak modes defined in Section 2.2, we use a few observables to quantify the properties of the detected galaxies using polar shapelet modes (Section 2.3.1). The galaxy properties studied here include flux (Section 2.3.2), size (Section 2.3.3) and shape (Section 2.3.4).

# 2.3.1 Polar shapelets

We construct galaxy properties corresponding to the flux, size, and shape out of combinations of shapelet modes. Shapelet modes are projections of the galaxy image signal onto a set of Gaussian weighted orthogonal functions (Refregier 2003; Massey & Refregier 2005). Furthermore, we derive the first-order shear responses of these galaxy properties using the shear responses of shapelet modes given by Massey & Refregier (2005). This is essential to deriving and correcting shear-estimation biases induced by galaxy selection process using the detected galaxy properties.

The polar shapelet basis functions (Massey & Refregier 2005; Bernstein & Jarvis 2002) are defined as

$$\chi_{nm}(\mathbf{x} \mid \sigma_{h}) = (-1)^{(n-|m|)/2} \left\{ \frac{\left[ (n-|m|)/2 \right]!}{\left[ (n+|m|)/2 \right]!} \right\}^{\frac{1}{2}} \\
\times \left( \frac{\rho}{\sigma_{h}} \right)^{|m|} L_{\frac{n-|m|}{2}}^{|m|} \left( \frac{\rho^{2}}{\sigma_{h}^{2}} \right) e^{-\rho^{2}/2\sigma_{h}^{2}} e^{-im\theta}, \tag{25}$$

where  $L_{\frac{n-|m|}{n-|m|}}^{|m|}$  are the Laguerre polynomials, n is the radial number and m is the spin number. n can be any non-negative integer, and m is an integer between -n and n in steps of two.  $\sigma_h$  determines the scale of shapelet functions in configuration space, which is set to the same scale as the Gaussian kernel used to smooth images in the detection process of Section 2.2.1.  $(\rho, \theta)$  is used to denote locations in 2D

polar coordinates, and the center of the coordinate system is set to the center of the peak of detected source, which does not have subpixel offsets. We scale the polar shapelet basis functions in Massey & Refregier (2005) by  $\sigma_h \sqrt{\pi}$  so that  $\chi_{00}(x)$  (which is an isotropic Gaussian function) is normalized to integrate to one:

$$\iint d^2x \chi_{00}(\mathbf{x}) = 1, \qquad (26)$$

and the re-smoothing kernel also integrates to one as the PSF integrates to one.

One important property of shapelet basis functions is that under a Fourier transform, the shapelet basis functions change as

$$\chi_{nm}(\mathbf{x} \mid \sigma_h) \longrightarrow \tilde{\chi}_{nm}(\mathbf{k}) = i^n \chi_{nm}(\mathbf{k} \mid 1/\sigma_h)$$
 (27)

The shapelet function in Fourier space,  $\tilde{\chi}_{nm}$ , has the same functional form as  $\chi_{nm}$  but the scale radius is the inverse of that of the function in configuration space (Refregier 2003).

We measure shapelet modes from galaxy light profiles in Fourier space after PSF deconvolution:

$$M_{nm} \equiv \iint \mathrm{d}^2 k \, \left( \tilde{\chi}_{nm}(k) \right)^* \frac{f_k^p}{p_k} \,. \tag{28}$$

Again, we set the scale radius of the Gaussian weight in shapelets,  $\sigma_h$ , to be greater than the scale radius of the PSF in configuration space. Note that we use an isotropic Gaussian kernel, and its size and shape are *not* adapted to those of the galaxies or PSFs. We do not adapt the basis functions to the size of the galaxy light profile, in order to simplify the derivation of shear responses of basis modes without assumptions regarding galaxy morphology. In real observations, we can separate the survey into small patches and choose a fixed smoothing scale,  $\sigma_h$ , for each patch.  $M_{00}$  is the same as the smoothed pixel value of the central peak; we refer to it as the FPFS peak value.

Note that the shapelet modes in this paper are different from the FPFS shapelet modes defined in Li et al. (2018, 2022b). Here we measure shapelet modes from the deconvolved galaxy profiles in Fourier space, rather than from the power of the galaxy's Fourier transform. The reason for this difference is as follows: The old FPFS method follows Zhang (2008) to avoid shear-dependent offcentering bias by measuring observables on the power in Fourier space after subtracting the average noise power (Zhang et al. 2015). In this paper, we set the peaks detected from images as the center of the coordinate system for the measurement. Since we derive the shear response of the peak detection, the anisotropy in the centering definition is corrected with the shear response. This non-power based estimator significantly simplifies the derivation of the covariance between different FPFS shapelet modes, not only from read noise and background photon noise, but also from source photon noise. We will expand and elaborate on this in Section 2.5.

Shapelet modes change when a galaxy image is distorted by a shear,  $\gamma_{1,2}$ . We use the transform formula for shapelets — equation (41) of Massey & Refregier (2005) — to derive the shear responses of the flux, size and shape defined in terms of shapelet modes. In summary, to the first order in shear, a *finite* number of shapelet modes (separated by  $|\Delta n|=2$  and  $|\Delta m|=2$ ) are coupled under shear distortion; therefore, one can write the shear response of any shapelet mode as a linear combination of a *finite* number of other shapelet modes (Li et al. 2018). As we will define galaxy size and shape using finite combinations of shapelet modes, their shear responses are also finite combinations of shapelet modes. It is worth mentioning that the FPFS shapelet modes are measured from deconvolved galaxies; therefore, PSFs do not bias the derivation, assuming that they are accurately determined at the positions of the galaxies.

#### 2.3.2 Galaxy flux

The zeroth order FPFS shapelet mode,  $M_{00}$ , is the value of the peak pixel, which can be used to quantity the brightness of galaxies. Since the re-smoothing kernel integrates to one, we define the FPFS flux as a rescaling of the peak value:

$$F = \frac{M_{00}}{\iint d^2k \left| \tilde{\chi}_{00}(\mathbf{k}) \right|^2 / |p_k|^2}, \tag{29}$$

where the denominator is the square of the  $L^2$  norm of the resmoothing kernel. F is the flux of the best fit re-smoothing kernel to the observed galaxy profile assuming the noise variance is a constant over the galaxy scale. This is mathematically similar to the prePSF Gaussian flux<sup>7</sup> proposed by Becker & Sheldon (prep).

On raw astronomical images before photometric calibration,  $M_{00}$  is in units of [photon counts per arcsec<sup>2</sup>]; in contrast, in this paper, we focus on coadded images of HSC / LSST after photometric calibration, and  $M_{00}$  is reported in units of [nano Jy arcsec<sup>-2</sup>]. Since the denominator in equation (29) is in unit of [arcsec<sup>-2</sup>], F is in unit of [nano Jy]. The FPFS magnitude is defined as

$$m_{\rm F} \equiv m_{\rm zero} - 2.5 \log(F) \,, \tag{30}$$

where  $m_{\rm zero}$  is the zero point of the survey (e.g., for HSC coadded images<sup>8</sup>, the zero point is 27). The galaxy number histogram as a function of FPFS magnitude for isolated galaxies in the simulation that will be introduced in Section 3.3.1 is shown in the top panel of Figure 3. When producing this figure, we do not run the detection or selection processes during the image processing, but rather tell the pipeline the centroids of the galaxies. In this paper, we refer to this setup as the forced-center setup.

Under a shear distortion,  $M_{00}$  (FPFS peak value) changes from its intrinsic value,  $\bar{M}_{00}$ , and the linear shear responses of the FPFS peak value for two shear components are

$$M_{00;1} = -\sqrt{2}M_{22c}, \qquad M_{00;2} = -\sqrt{2}M_{22s},$$
 (31)

where  $M_{22c}$  and  $M_{22s}$  refer to the real ('cos') and imaginary ('sin') components of the complex shapelet mode  $M_{22}$ , respectively. These shear responses for the FPFS peak value will be used to derive the shear response of the galaxy detection/selection using the FPFS magnitude and to correct the detection/selection bias induced by the shear-dependence of  $M_{00}$  in Section 2.4.2.

In Figure 4, we show the relationship between the FPFS magnitude and the other magnitudes measured by the HSC pipeline (Bosch et al. 2018) on noiseless, isolated galaxies with HSC-like pixel scale (0'.168) and seeing size (0'.59). The Gaussian shapelet kernel used to measure  $M_{00}$  has a FWHM of 1'.4. The FPFS galaxy magnitudes are fainter than the CModel magnitudes by about 0.3 magnitude on average since the effective aperture scale of the shapelets Gaussian kernel is less than the typical galaxy scale; as a result, not all of the light from galaxies is included in the effective PSF-deconvolved Gaussian window. The aperture magnitudes with diameter 1'.5 have the smallest average offset from and least scatter with respect to the FPFS magnitudes. This is because the aperture size is close to the effective smoothing scale of re-smoothing kernel adopted by the FPFS magnitudes.

# 7 https://github.com/esheldon/ngmix

#### 2.3.3 Galaxy size

Second-order Gaussian weighted moments are widely used to quantify the size of galaxies (see, e.g., Hirata & Seljak 2003). We decompose the spin-0 second-order radial moment as a combination of shapelet modes:

$$\iint d^2x \, f_x \left(\frac{\rho}{\sigma_h}\right)^2 e^{-\rho^2/2\sigma_h^2} = M_{00} + M_{20} \,, \tag{32}$$

and define the FPFS resolution using shapelet modes:

$$R_2 \equiv \frac{M_{00} + M_{20}}{M_{00}} \,. \tag{33}$$

Note that this shapelet resolution is conceptually similar to the reGauss resolution defined in Hirata & Seljak (2003). The galaxy number histogram as a function of FPFS resolution for the isolated galaxy image simulations with the forced-center setup, which assumes the galaxies' centroids are known during the image processing, is shown in the lower panel of Figure 3.

Since the shear responses of  $M_{20}$  for the two shear components are

$$M_{20:1} = -\sqrt{6}M_{42c}$$
,  $M_{20:2} = -\sqrt{6}M_{42s}$ , (34)

according to Massey & Refregier (2005), the linear shear responses of the FPFS resolution can be derived with equation (31):

$$R_{2;1} = \sqrt{2} \left( \frac{M_{22c} M_{20}}{(M_{00})^2} \right) - \sqrt{6} \frac{M_{42c}}{M_{00}} ,$$

$$R_{2;2} = \sqrt{2} \left( \frac{M_{22s} M_{20}}{(M_{00})^2} \right) - \sqrt{6} \frac{M_{42s}}{M_{00}} .$$
(35)

#### 2.3.4 Galaxy ellipticity

We define galaxy ellipticity as

$$e_1 \equiv \frac{M_{22c}}{M_{00} + C}, \qquad e_2 \equiv \frac{M_{22s}}{M_{00} + C}.$$
 (36)

The weighting parameter C, introduced by Li et al. (2018), adjusts the relative weight between galaxies with different brightness; moreover, it ensures that the second-order noise bias in equation (7) is the leading-order term and we can neglect the higher-order terms. While this ellipticity definition follows the basic form suggested by Li et al. (2018), it differs in that this ellipticity is measured from the galaxy's Fourier transform, rather than from the Fourier power.

To the first order in shear,  $e_{\alpha}$  transforms under the shear distortion, where  $\alpha, \beta \in \{1, 2\}$ , as follows:

$$\bar{e}_{\alpha} \to e_{\alpha} = \bar{e}_{\alpha} + \sum_{\beta=1,2} e_{\alpha;\beta} \gamma_{\beta},$$
 (37)

and the *shear response* matrix is  $e_{\alpha\beta} \equiv \partial e_{\alpha}/\partial \gamma_{\beta}$  (Huff & Mandelbaum 2017). In Li et al. (2018), we use the linear shear responses of shapelets given by Massey & Refregier (2005) to derive the expectation values of the diagonal elements of the matrix:

$$\langle e_{\alpha;\alpha} \rangle = \frac{1}{\sqrt{2}} \left\langle s_0 - s_4 + 2e_\alpha^2 \right\rangle,$$
 (38)

where  $s_{0,4}$  are spin-0 properties:

$$s_0 \equiv \frac{M_{00}}{M_{00} + C}, \qquad s_4 \equiv \frac{M_{40}}{M_{00} + C}.$$
 (39)

The off-diagonal terms of the matrix are composed of spin-4 shapelet modes, which go to zero when averaging over a large number of galaxies if the selection of the galaxy sample does not cause any spin-4 leakage.

<sup>&</sup>lt;sup>8</sup> Coadded images are the weighted sum of images (after smoothing with a warping kernel) from multiple visits at the same position in the same optical band (Bosch et al. 2018).

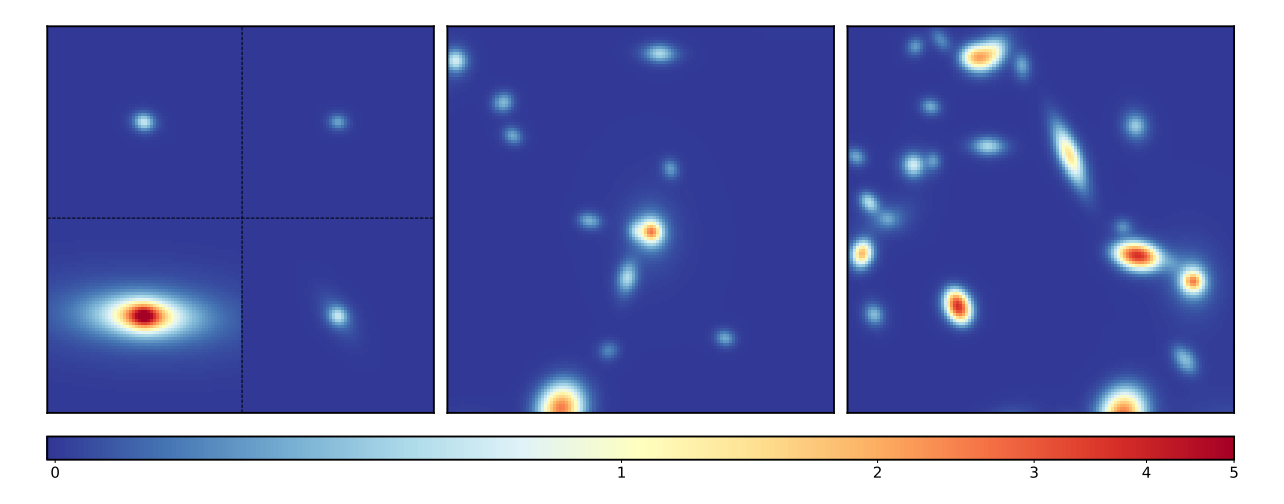


Figure 6. The left panel shows a 128 pix  $\times$  128 pix (or, equivalently,  $0.36 \times 0.36$  arcmin<sup>2</sup>) region of the isolated stamp-based galaxy image simulation, where the black lines indicate the boundaries of the 64 pix  $\times$  64 pix stamps. The middle and the right panels are for blended galaxy image simulations with input densities of 85 arcmin<sup>-2</sup> and 170 arcmin<sup>-2</sup>, respectively. The images shown here are noiseless for demonstration, but different noise realizations are added to the galaxy images during the tests of shear estimation.

The definitions of ellipticity, in equation (36), and its shear response, equation (38), indicate that their expectation values go to zero for a star sample if the PSF is precisely and accurately modelled. Moreover, as shown in Figure (8) of Li et al. (2022b), our noise bias correction can remove the non-zero second-order term of measurement error,  $(\delta e_{\alpha})^2$  in the shear response. Therefore, stellar contamination in the galaxy sample should not bias shear estimation.

This shear response of the ellipticity,  $\langle e_{\alpha;\alpha} \rangle$ , can only be used to estimate the ensemble weak-lensing shear if there is no shear-dependent detection/selection, shear-dependent weighting, or image noise. The shear estimator for this over-simplified case is

$$\widehat{\gamma}_{\alpha} = \frac{\langle e_{\alpha} \rangle}{\langle e_{\alpha;\alpha} \rangle}, \tag{40}$$

and we will revisit this in detail when deriving corrections for detection and selection biases in Section 2.4.

#### 2.4 Shear response of detection/selection

We define the selection weight functions, w in equation (1), corresponding to cuts on FPFS peak modes (Section 2.2.1), FPFS magnitude (Section 2.3.2) and FPFS resolution (Section 2.3.3), respectively. The cuts on the peak modes are used to identify peaks in images as galaxy candidates; the cuts on FPFS peak flux and resolution are used to select galaxies that are sufficient for weak-lensing science. Normally, cuts on peak modes are regarded as part of the galaxy detection process, and cuts on magnitude and resolution are regarded as part of the galaxy sample selection process. For our purpose we describe these using a common formalism and treat them both as a form of selection.

We begin from selection using one observable following Li et al. (2022b) in Section 2.4.1, and then generalize the formalism to cuts on multiple observables in Section 2.4.2.

#### 2.4.1 One-observable selection

In Li et al. (2022b), we analytically derived and corrected for the selection bias caused by a hard cut on one observable,  $\nu$ :

$$v > \mu, \tag{41}$$

by studying how the edge of the cut changes under shear distortion. A different approach is adopted here: we follow the formalism introduced in Section 2.1.2 to derive the detection/selection bias correction by considering how the histogram of galaxy properties is shifted under a shear distortion.

Following Kaiser (2000), we interpret a hard cut on one observable as a Heaviside step selection weight applied to the galaxy sample:

$$w_{\rm H}(v) = \begin{cases} 1 & \text{if } v > \mu \\ 0 & \text{if } v \le \mu \end{cases}$$
 (42)

From equations (4) and (6), the shear dependency of the selection weight leads to an additional anisotropy that is proportional to the shear:

$$\Delta \langle w e_{\alpha} \rangle_{\text{sel}} = \gamma_{\alpha} \iint de \, dv \, \mathcal{P}(e, v) \frac{\partial w_{\text{H}}(v)}{\partial v} \frac{\partial v}{\partial \gamma_{\alpha}} e_{\alpha} \,, \tag{43}$$

where  $\mathcal{P}(e, v)$  is the 2D PDF of the galaxy sample. Since  $\partial w(v)/\partial v = \delta_{\rm D}(v - \mu)$ , where  $\delta_{\rm D}$  is the Dirac delta function, we have

$$\Delta \langle w e_{\alpha} \rangle_{\text{sel}} = \gamma_{\alpha} \left. \mathcal{P}(v) \right|_{v=\mu} \left\langle e_{\alpha} \frac{\partial v}{\partial \gamma_{\alpha}} \right\rangle \right|_{v=\mu}, \tag{44}$$

where  $\mathcal{P}(v)|_{v=\mu}$  is the marginal PDF at  $v=\mu$ . Equation (44) is identical to equation (31) of Li et al. (2022b), although we derive them from different perspectives.

#### 2.4.2 Multi-observable selection

In real observations, we need to apply cuts on multiple galaxy properties. However, we find that the correction for noise bias in equation (44) is very noisy and unstable especially when applying a hard selection weight function to multiple galaxy cuts. This instability arises because the hard selection weight,  $w_{\rm H}$ , is discontinuous at the

selection boundary, and the estimate of the marginal number density at multiple cuts is unstable. To address this issue, we explore whether the application of a selection weight that is differentiable, corresponding to a soft cut, might make the process of correcting for the selection bias due to multiple cuts more stable.

The sigmoid function is a smooth function with continuous derivatives up to infinite order (as indicated by the subscript in  $w_{\infty}$ ):

$$w_{\infty}(v \mid \omega) = \frac{1}{1 + \exp\left(-\frac{v}{\omega}\right)},\tag{45}$$

which is used to avoid the discontinuity in the hard selection function. The parameter  $\omega>0$ , which we refer to as the smoothness parameter, changes the average slop of the sigmoid function — the sigmoid function approaches a step function as  $\omega$  approaches 0. However, the sigmoid function is not compact — that is, it does not go precisely to zero even for  $\nu\ll0$ .

We propose to use a truncated sine function for the selection weight:

$$w_{2}(v \mid \omega) = \begin{cases} 0 & \text{if } v \in (-\infty, -\omega) \\ \frac{1}{2} + \frac{v}{2\omega} + \frac{1}{2\pi} \sin\left(\frac{v\pi}{\omega}\right) & \text{if } v \in [-\omega, \omega] \\ 1 & \text{if } v \in (\omega, +\infty) \end{cases}$$
 (46)

This truncated sine function has continuous derivatives up to second-order (as indicated by the subscript in  $w_2$ ), and it goes precisely to zero below  $-\omega$ . The hard, sigmoid and truncated sine selection functions and their first-order derivatives are shown in Figure 5. The compactness of the truncated sine function enables us to neglect the galaxies with observable  $v < -\omega$  during the detection and selection process.

We define the cut on peak modes,  $q_i$ , where  $i \in \{0, ..., 7\}$ , with a smoothness parameter  $\omega_a$ , as

$$w_{\mu_q \omega_q} = \prod_{i=0}^{7} w_2 (q_i - \mu_q M_{00} - \omega_q \mid \omega_q).$$
 (47)

For this selection, the mean cutoff is  $\mu_q M_{00} + \omega_q$ , and the width is  $\omega_q$ , so that this soft cut removes all galaxies with  $q_i < \mu_q M_{00}$  and select peaks from the image. In addition, this cut downweights galaxies between  $\mu_q M_{00}$  and  $\mu_q M_{00} + 2\omega_q$ . Note that here we introduce  $\mu_q M_{00}$  to avoid false detections near bright sources. We fix  $\mu_q$  to a small value  $(5 \times 10^{-3})$  in this paper.

For a cut on FPFS magnitude,  $m_F$ , at  $\mu_m$ , with a smoothness parameter  $\omega_m$ , the selection weight function is given by

$$w_{\mu_m \omega_m} = w_2 \left( F - 10^{\frac{m_{\text{zero}} - \mu_m}{2.5}} \mid \omega_m \right). \tag{48}$$

Note that to reduce one level of non-linearity, we transform the cut on magnitude into a cut on F, which is a linear function of the image signal. The mean cutoff on F is  $10^{\frac{m_{ECO}-\mu_m}{2.5}}$ , and the cutoff width is  $\omega_m$ .

For a cut on FPFS resolution,  $R_2$ , at  $\mu_R$ , with a smoothness parameter  $\omega_R$ , the selection weight function is given by

$$w_{\mu_R \omega_R} = w_2 \left( M_{20} + (1 - \mu_R) M_{00} \,|\, \omega_R \right) \,. \tag{49}$$

Here, too, we reduce one level of non-linearity by transforming the cut on resolution,  $R_2$ , into a cut on  $M_{20} + (1 - \mu_R)M_{00}$ , which is a linear function of the image signal. Following its definition, a cut on FPFS resolution at  $\mu_R$ :

$$\frac{M_{20} + M_{00}}{M_{00}} > \mu_R \tag{50}$$

is equivalent to a cut:

$$M_{20} + (1 - \mu_R)M_{00} > 0. (51)$$

Then we approximate this hard cut on the linear observable,  $M_{20}$  +  $(1 - \mu_R)M_{00}$ , with the soft truncated sine function.

The final selection weight used to select the galaxy sample is

$$w = w_{\mu_q \omega_q} w_{\mu_m \omega_m} w_{\mu_R \omega_R} . \tag{52}$$

Since we have calculated the first order shear responses of peak modes and shapelet modes in Sections 2.2 and 2.3, we can derive the derivative of the selection weight function to shear. Therefore, the shear response of the average of weighted ellipticity with the correction for shear-dependent detection/selection bias *in the absence of noise* can be derived following equation (6), and the shear estimator is

$$\widehat{\gamma}_{\alpha} = \frac{\langle w e_{\alpha} \rangle}{\langle w e_{\alpha;\alpha} + w_{;\alpha} e_{\alpha} \rangle}, \tag{53}$$

where  $e_{\alpha}$  is defined in equation (36) and  $e_{\alpha;\alpha}$  is in equation (38).

Our method of correction for detection and selection bias differs from that of Metadetection (Sheldon et al. 2020). They correct for biases from shear-dependent detection and selection by shearing each galaxy image and rerunning the detection and selection processes. In contrast, we adopt a coordinate-based approach by analytically deriving the basis functions' shear responses, which is functionally equivalent to shearing the basis functions (but analytically rather than via a numerical re-simulation process). However, the common aspect to these approaches is that they seek an empirical correction for selection and detection biases, rather than relying on calibration from simulations.

#### 2.5 Covariance of measurement error

The shear estimator in equation (53) neglects the bias from image noise. Due to the non-linearity in the galaxy ellipticity and selection weight, image noise biases both the measured ellipticity and the selection weight. In order to estimate the second-order noise bias corrections for the observables in equation (53) (e.g., the noise bias correction for the average of weighted ellipticity in equation (9)), we analytically derive the covariance of the measurement errors on the basis modes defined in Section 2.2 (peak modes) and 2.3 (shapelet modes).

We denote the image noise in configuration space and Fourier space as  $n_x$  and  $n_k$ , respectively. Here we focus on noise fields that are homogeneous on the length scales of galaxies, but that have pixel-to-pixel correlations. Image noise on coadded images of ground-based observations (e.g., HSC and LSST) is approximately homogeneous on the length scales of typical galaxies, since the image noise of ground-based observations is dominated by sky background noise, which varies on larger scales. The correlation of noise between pixels is caused by the warping kernel when resampling the images to a common pixel grid in the coaddition process (see, e.g., Bosch et al. 2018). Noise correlation on single exposures can also be caused by the brighter-fatter effect and inter-pixel capacitance of CMOS detector (Givans et al. 2022). Additionally, undetected faint galaxies can effectively also lead to correlation across pixels (Eckert et al. 2020).

The noise homogeneity on galaxy length scales means that there is no correlation between the noise on different wave numbers in Fourier space. The Fourier power spectrum of noise is denoted as  $N_k$ , and the covariance of noise in Fourier space is

$$\langle n_k n_{k'}^* \rangle = N_k \delta_{\rm D}(\mathbf{k} - \mathbf{k}') \,, \tag{54}$$

where  $\delta_{\rm D}$  is the Dirac delta function.

Since the FPFS basis modes are linear functions of images, the

corresponding measurement errors are the noise projected onto the shapelet bases after deconvolution:

$$\delta M_{nm} = \iint d^2k \left( \tilde{\chi}_{nm}(\mathbf{k}) \right)^* \frac{n_k}{p_k}$$

$$\delta q_{\mathbf{x};\alpha} = \iint d^2k \left( \psi_{\mathbf{x};\alpha}(\mathbf{k}) \right)^* \frac{n_k}{p_k}.$$
(55)

Taking the covariances between shapelet modes  $M_{nm}$  and  $M_{n'm'}$  as an example, the covariances are

$$K_{M_{nm}}^{M_{n'm'}} \equiv \langle \delta M_{nm} \delta M_{n'm'}^* \rangle = \iint d^2 k \, \tilde{\chi}_{nm}^* \tilde{\chi}_{n'm'} \frac{N_k}{P_k} \,. \tag{56}$$

In the real observations, these covariances can be estimated if we can measure the noise power function,  $N_k$ , from blank pixels, and the Fourier power function of PSF,  $P_k$ , from the PSF model:

$$P_k = p_k p_k^* \,. \tag{57}$$

The covariance between the other basis modes has the same form. It is worth noting that the covariances of measurement errors do not depend on galaxy properties, unlike those derived from the galaxy Fourier power in Li et al. (2022b). Moreover, the above equations do not assume that the noise is Gaussian.

It is worth noting that, for images of space-based observations, image noise is dominated by galaxy photon noise that is not homogeneous. As we show in Appendix D, the covariances of basis modes can be analytically derived for inhomogeneous noise if it does not have pixel-to-pixel correlation. This is approximately true for single exposures of space-based observations, as noise on single exposures has very small pixel-to-pixel correlations. This paper focuses on homogeneous noise; we leave the discussion of inhomogeneous noise to our future work.

# 2.6 Shear estimation recipe

Finally, we summarize the process of applying our shear estimator defined in equation (10) with our specific implementation of ellipticity and selection weights. This code for the pipeline is public<sup>9</sup>, and it can carry out the detection, selection, and shear measurement for  $\sim 1000$  galaxies per CPU second.

We briefly summarize the pipeline for ensemble shear estimation as follows:

- (i) Carry out a loose preselection of peaks as galaxy candidates after PSF deconvolution and re-smoothing with a target Gaussian kernel;
- (ii) Compute the selection weight defined in equation (52) for each preselected peak. This selection weight is constructed with shapelet modes (Section 2.3.1) and peak modes (Section 2.2.3) and used for the postselection of galaxies sufficient for weak-lensing science;
- (iii) Measure the spin-2 ellipticity defined in equation (36) for each postselected galaxy. The ellipticity is constructed with shapelet modes (Section 2.3.1);
- (iv) Estimate the shear response of the ellipticity according to equation (38) and the shear response of the selection weight following Section 2.4.2. These estimates use the shear responses of shapelet modes (equations (31) and (34)) and those of peak modes equation (24);
- (v) Estimate the shear response of the average weighted ellipticity using equation (6);

- (vi) Correct for the noise biases in the expectation values of the weighted ellipticity and its shear response following equations (C2)–(C4). The noise bias correction uses the covariance matrix of measurement errors on basis modes introduced in Section 2.5 and the Hessian matrix of the ellipticity and its shear response as functions of basis modes summarized in Appendix C;
- (vii) Shear is estimated with equation (10), which incorporates corrections for detection and selection bias, and for noise bias.

#### **3 IMAGE SIMULATION**

We test the performance of the shear estimator after correcting for noise bias, selection bias and detection bias by analyzing mock astronomical images that have been distorted by known input shears. The estimated shear,  $\widehat{\gamma}_{1,2}$ , is related to the input shear,  $\gamma_{1,2}$ , as

$$\widehat{\gamma}_{1,2} = (1 + m_{1,2}) \gamma_{1,2} + c_{1,2}, \qquad (58)$$

where  $m_{1,2}$  (multiplicative bias) and  $c_{1,2}$  (additive bias) are used to quantify the accuracy of the shear estimator (Huterer et al. 2006; Heymans et al. 2006).

#### 3.1 Galaxies, PSF and noise

Galaxy images are generated using the open-source package GalSim (Rowe et al. 2015). We use the COSMOS HST Survey catalogue<sup>10</sup> (Mandelbaum et al. 2012) with limiting magnitude F814W = 25.2 as our input galaxy catalog. The galaxies' light profiles are approximated with the best-fitting single Sérsic model (Sérsic 1963) or two-component bulge-disk model (with the bulge component following de Vaucouleurs 1948). This parametric galaxy catalogue can be used directly for image rendering by GalSim (for details, see Mandelbaum et al. 2014). We truncate each input parametric galaxy model at five times its half-light radius. Each parametric model is expanded by a random number uniformly distributed between 0.95 and 1.05 to change its size, while not adjusting its flux. Then galaxies are rotated by a random angle before they are distorted by the input shear.

The pixel scale is set to 0'.168, which is the pixel scale of HSC coadded images. For these simulations, the PSF image is modelled with a Moffat (1969) profile,

$$p_m(\mathbf{x}) = \left[1 + c\left(\frac{|\mathbf{x}|}{r_{\rm P}}\right)^2\right]^{-3.5},\tag{59}$$

where  $c = 2^{0.4} - 1$  and  $r_P$  is set such that the full width half maximum (FWHM) of the PSF is 0″.60, matching the mean seeing of the HSC survey in the *i*-band (Li et al. 2022a). However, we note that the Moffat PSF profile is different from the actual PSFs in HSC. We use the HSC pipeline to measure the FWHM of the input Moffat PSF with a Gaussian weighted moment, and the resulting FWHM is 0″.65 . The difference between the input FWHM and measured FWHM is due to the fact that the measurement algorithm assumes a Gaussian profile. The PSF profile is truncated at a radius four times of its FWHM. In order to test whether our algorithm can remove shear estimation bias from PSF anisotropy, we shear the PSF so that it has ellipticity ( $e_1 = 0.02$ ,  $e_2 = -0.02$ ).

We add image noise composed of photon noise from a constant sky background and read noise, neglecting the contribution of photon noise from galaxy. This is because photon noise from the sky

<sup>9</sup> https://github.com/mr-superonion/FPFS

<sup>10</sup> https://zenodo.org/record/3242143#.YPBGdfaRUQV

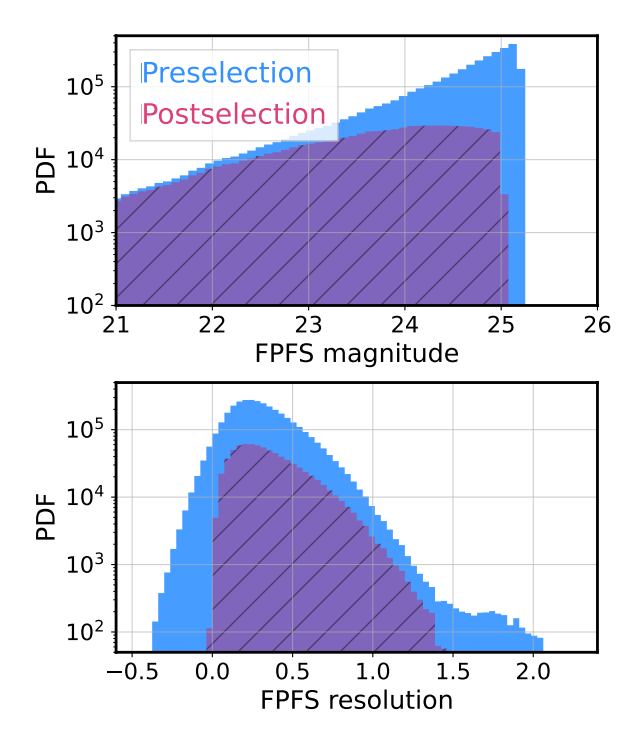


**Figure 7.** The FPFS magnitude ( $m_F$ ; defined in equation (30)) and FPFS resolution ( $R_2$ ; defined in equation (33)) distributions for the preselection (unhatched) and postselection (hatched) galaxy samples from the stamp-based image simulations, where galaxies have a random subpixel offset from stamp's center.

background dominates over that from galaxies for ground-based observations. We leave detailed treatment of source Poisson noise to future work. Our noise model includes anisotropic correlation between pixels matching the autocorrelation function of a third-order Lanczos kernel, i.e., a = 3 in

$$L(x,y) = \begin{cases} \operatorname{sinc}\left(\frac{x}{a}\right) \operatorname{sinc}\left(x\right) \operatorname{sinc}\left(\frac{y}{a}\right) \operatorname{sinc}\left(y\right) & \text{if } |x|, |y| < a \\ 0 & \text{otherwise,} \end{cases}$$
 (60)

where  $sinc(x) = sin(\pi x)/\pi x$ . This kernel was used to warp and coadd exposures for the HSC survey dataset (Bosch et al. 2018). Ignoring pixel-to-pixel correlations, our resulting noise variance is  $7 \times 10^{-3}$  nano Jy, which is approximately two times the average noise variance on HSC coadds in Li et al. (2022a). We chose this higher noise level to ensure that our algorithm can be applied to the HSC survey even for its noisiest images.

#### 3.2 Shape noise and image noise cancellation

To reduce the intrinsic shape noise in our tests, enabling us to tightly constrain shear biases with fewer simulations, we generate two images for each galaxy distorted by different shears —  $(\gamma_1 = 0.02, \gamma_2 = 0)$  and  $(\gamma_1 = -0.02, \gamma_2 = 0)$ . However, the images share exactly the same realisation of image noise (following Pujol et al. 2019; Sheldon et al. 2020). In addition, we force our galaxy sample to contain orthogonal galaxies with the same morphology and brightness but the major axes rotated by 90 deg following Massey et al. (2007).

To measure the shear measurement bias defined in equation (58),

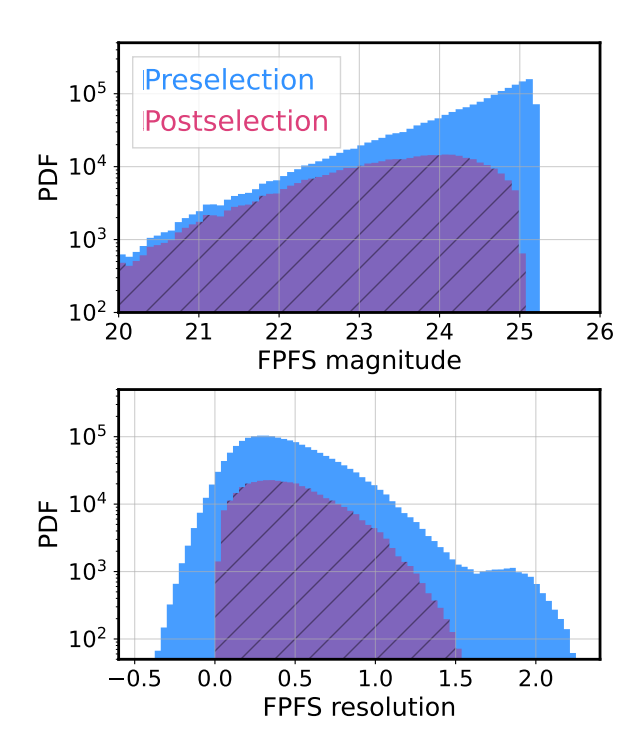


**Figure 8.** Same as Figure 7, but for galaxies in the blended image simulation with input number density 85 arcmin<sup>-1</sup>.

we measure multiplicative bias and additive bias as

$$c_1 = \frac{\langle \widehat{we_1}^+ + \widehat{we_1}^- \rangle}{(\widehat{\mathcal{R}}_1^+ + \widehat{\mathcal{R}}_1^-)} \tag{61}$$

and

$$m_1 = \frac{\langle \widehat{we_1}^+ - \widehat{we_1}^- \rangle}{0.02(\widehat{\mathcal{R}}_1^+ + \widehat{\mathcal{R}}_1^-)} - 1, \qquad (62)$$

where  $\widehat{we_1}^+$  and  $\widehat{\mathcal{R}}_1^+$  are the first component of the weighted ellipticity and the shear response for its expectation value, respectively. They are estimated from the images distorted by the positive shear,  $(\gamma_1 = 0.02, \gamma_2 = 0)$ .  $\widehat{we}_1^-$  and  $\widehat{\mathcal{R}}_1^-$  are from images with the negative applied shear,  $(\gamma_1 = -0.02, \gamma_2 = 0)$ . The bias estimators in equations (61) and (62) assume that  $\widehat{\mathcal{R}}_1^+ = \widehat{\mathcal{R}}_1^-$  which is true for our simulation since the input galaxy sample is the same for the images with positively and negatively distorted galaxies. For these very well-sampled images, anisotropy in the horizontal/vertical versus diagonal directions due to the pixel response function is considered to be part of the effective PSF. Given that our correction for the impact of PSF dilution on shear inference is accurate, the multiplicative and additive biases we find for  $\widehat{\gamma}_2$  should be comparable to those for  $\widehat{\gamma}_1$ . Therefore, we only confirm that the results for  $\widehat{\gamma}_2$  are consistent with those for  $\widehat{\gamma}_1$  for noiseless images. To save computational time, we do not test the noise bias correction for estimation of  $\widehat{\gamma}_2$ , which requires a large number of additional image simulations. It is worth noting that this testing scheme reduces statistical error in multiplicative bias due to image noise. The errors on the means of multiplicative bias and additive bias are estimated with jackknife resampling of the galaxies.

The galaxies in each orthogonal galaxy pair and galaxies with different applied shears are selected (weighted) independently, and we apply the shear estimator to the selected sample to test our corrections for detection bias and selection bias.

#### 3.3 Isolated and blended setups

We prepare both isolated and blended image simulations so that we can separately quantify the shear estimation biases for isolated galaxies and those related to blending.

#### 3.3.1 Isolated galaxies

For the isolated image simulations, we randomly select galaxies from the HST parametric galaxy catalogue. After the shear distortion and PSF convolution, galaxies are rendered in 64 × 64 pixel postage stamp images. The convolved galaxies are further truncated by the boundaries of their postage stamp. Each simulated image contains 100 × 100 postage stamps, and each postage stamp contains an isolated galaxy randomly selected from the input COSMOS galaxy sample with replacement (each galaxy is selected repeatedly). Each image has  $5 \times 10^3$  orthogonal galaxy pairs with identical morphologies and fluxes, but with major axis directions separated by 90 deg. We show a small region of one simulated image in the left panel of Figure 6. We prepare simulations with two setups: one puts the galaxy centroid at the center of each postage stamp; the other shifts galaxies with random sub-pixel offsets. For each setup, we generate 3000 images with different realizations for the image noise, galaxy sample, random galaxy rotation and size expansion factor. Galaxies in each of the images are distorted by  $\gamma_1 = \pm 0.02$ , meaning that there are two versions of each image.

We run the FPFS detection and selection process on 200 of the 3000 simulated stamp-based images, and show the preselection and postselection galaxy number histograms as functions of FPFS magnitude and resolution in Figure 7. As mentioned in Section 2.2.3, the preselection process applies hard cuts on the re-smoothed pixel values and FPFS magnitude using loose threshold values:  $q_i >$ -0.12 [nano Jy] and  $m_{\rm F}$  < 25.2. However, the postselection process is a soft selection with stricter thresholds on magnitude, peak modes and resolution to select galaxies that are sufficient for weaklensing science, as defined in Section 2.4.2. The smoothness parameters for the soft postselection are set to  $\omega_q = 0.2$  [nano Jy],  $\omega_R = 0.2$  [nano Jy] and  $\omega_m = 0.2$  [nano Jy], and the cutoff centers for magnitude and resolution are  $m_{\rm F}=25$  and  $R_2=0.05$ . Note that we do not add a very conservative resolution cut since we are not particularly worried about star contamination in our shear estimation since, as shown in Figure (8) of Li et al. (2022b), the ellipticity and shear response of noisy stars all average to zero. The magnitude cut corresponds to SNR~12.5. In the following tests, we apply these soft cuts for galaxy detection and selection by default.

#### 3.3.2 Blended galaxies

For the simulations to test the impact of blending, the HST parametric galaxies are rendered into random positions on the images instead of dividing images into postage stamps. We generate 10<sup>4</sup> images with different realizations for the galaxy sample, galaxy positions, random rotation angle, size expansion factor and image noise. The galaxies are evenly distributed within a circle centered at the image's center. The size of the image is designed to be 10% larger than the diameter of the circle. The number density of the input galaxies

is set to 85 arcmin<sup>-2</sup>, which is similar to the default setup of MacCrann et al. (2022). In Li et al. (2022a), we checked that the number density of galaxies with CModel magnitude brighter than 24.5 and reGauss resolution greater than 0.3 detected from simulations with this input galaxy number density matches the number density of the magnitude-limited galaxy sample in the HSC survey. In addition, we produce images with a higher number density, 170 arcmin<sup>-2</sup>, for an approximate stress test of the algorithm under extreme conditions (e.g., near the center of a galaxy cluster – albeit without attempting to simulate in detail the different galaxy population that would be present in a cluster). The center of the shear distortion is fixed to the image center, so that it changes both the shape and position of each galaxy. The images of blended galaxy simulations with different number densities are shown in the middle and right panel of Figure 6.

It is worth noting that MacCrann et al. (2022) tested Metacalibration using simulations with redshift-dependent shear by dividing galaxies into four redshift bins and applying different shears to galaxies in each bin. They found that blended galaxies at different redshifts change the galaxies' effective number density distribution as a function of redshift since the shape measured from one galaxy contains information from other galaxies blended with the measured one but located at different redshifts. However, in this paper, we do not investigate the changes in effective redshift distribution, and only focus on the case that all galaxies in one image are distorted by the same shear. In addition, we do not include clustering in the galaxy's spatial distribution. With clustering, it is more likely for blended galaxies to be located in the same redshift bin; therefore, clustering can change the effective redshift distribution. However, we leave the tests related to redshift-dependent shear to the future work.

We run the FPFS detection and selection process on 200 images of the blended image simulation with input galaxy number density  $85 \text{ arcmin}^{-1}$ , and we show the preelection and postselection galaxy number histograms as functions of FPFS magnitude and resolution in Figure 8. Comparing the bottom panels of Figures 7 and 8, we find that for the blended image simulation, there are many preselection galaxies with extremely large resolution and there is a secondary peak in the resolution histogram at  $R_2 = 2$ . Many of these extremely large galaxies are false detections near bright sources. However, those galaxies in the secondary peak are removed after the postselection since we have a conservative cut on peak modes as shown in equation (47).

# 4 RESULTS

# 4.1 Isolated galaxies

In this subsection, we focus on isolated galaxies simulated within postage stamps (Section 3.3.1). We test the FPFS shear estimator under two different conditions. For the first setup, we do not run the FPFS detection process, but rather place each galaxy at the center of the postage stamp and force a measurement for each galaxy based on that known center. We test the correction for noise bias on galaxy shape estimation without applying any cut on the galaxy sample, and then we apply flux- and resolution-based selection criteria to the galaxy sample to test our corrections for selection biases. For the second setup, each galaxy has a random sub-pixel offset from the center of the postage stamp, and we run the FPFS peak detection algorithm and measure galaxy properties using the detected peak as the centroid. We apply flux- and resolution-based selection criteria to the detected galaxy sample and compare the results with those for

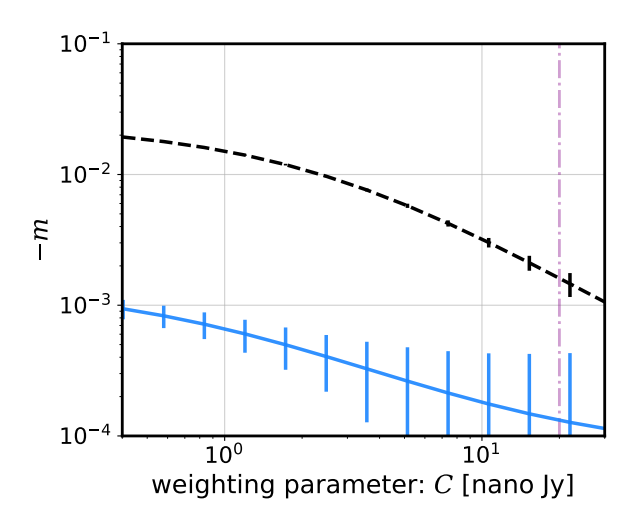


Figure 9. The multiplicative bias caused by image noise (i.e., noise bias) as a function of weighting parameter, C. The solid and dashed lines show the results with and without the second-order noise bias correction, respectively. All measured multiplicative biases are negative. The gray region denotes the LSST ten-year requirement on the control of multiplicative bias, which is defined for redshift-dependent multiplicative bias (The LSST Dark Energy Science Collaboration et al. 2018). For this figure, galaxies are isolated, and no detection or selection processes were carried out, which has enabled us to isolate the impact of noise bias more specifically. The vertical dash-dotted line is the default value for C.

the forced-center condition, to isolate the biases related to galaxy detection.

#### 4.1.1 Forced center

We first use the forced-center simulations to test the noise bias correction without galaxy selection and detection. We will use our results to set the parameter C, which enters into the denominator of the ellipticity definition in equation (36). To be more specific, we use all of the galaxies in the simulation by setting the selection weight function, w, to 1 for all galaxies. As shown in Figure 9, after the secondorder noise bias correction with equation (9), the amplitudes of multiplicative biases are reduced by at least one order of magnitude. In addition, the noise biases, both before and after the second-order correction, decrease as functions of the weighting parameter, C. This is consistent with the mathematical derivation in Li et al. (2022b): the noise bias residuals are proportional to the second and fourth powers of  $\delta M_{nm}/(M_{00}+C)$  before and after the second-order correction, respectively. We find that the additive bias is below  $10^{-4}$  for both corrected and uncorrected shear estimators when C > 1 [nano Jy]; therefore, we do not plot the additive bias here.

According to Li et al. (2018), not only the accuracy, but also the precision of the estimated shear, depends on the weighting parameter, C. As shown in Figure 10, the shape noise increases as a function of C, whereas the measurement error due to image noise decreases as a function of C. The trends are consistent with what we found in Figure (3) of Li et al. (2022b). Note, since the non-power-based shear estimator adopted here has lower measurement error compared to the power-based shear estimator adopted in Li et al. (2022b), the total statistical uncertainty (including both shape noise and measurement error) reduces by about 6%. To focus on the shear

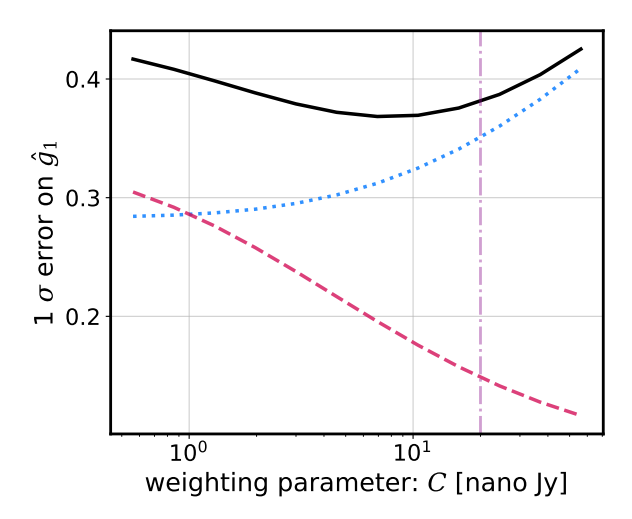


**Figure 10.** The  $1\sigma$  statistical uncertainty on shear measurements  $\widehat{\gamma}_1$  at the individual galaxy level (solid line), as a function of weighting parameter, C. The total uncertainty has contributions due to measurement error (dashed line) and intrinsic shape noise (dotted line). We separate shape noise from measurement error using noisy galaxy images and the corresponding noiseless galaxy images. The vertical dash-dotted line is the default setup for C.

estimation bias from detection and sample selection, we conservatively set the default weighting parameter for the following tests to C = 20 [nano Jy], with the intention of controlling the noise bias in the shear estimates to the level of  $\sim 1 \times 10^{-4}$ . As shown in Figure 10, this choice only increases the statistical uncertainty by 5% from the optimal value.

In Figures 11 and 12, we apply different selections on FPFS magnitude and FPFS resolution to select samples from the simulated galaxies, and run the shear estimator on the selected samples with and without correction for selection bias (including noise bias in the selection). For both cases, noise biases in the ellipticity,  $\tilde{e}_{\alpha}$ , and in its shear response,  $\tilde{e}_{\alpha;\alpha}$ , are corrected. As discussed in Section 2.4.2, we are not using hard cuts for galaxy sample selection but rather a soft selection weight defined in equation (46) to approximate the normal hard selection cut. Since our adopted selection weight is differentiable up to second order, the second-order selection bias from the soft selection cut can be analytically corrected very effectively. The characteristics of the detected sample given the default setup of the soft selection used here are shown in Figure 7.

We find the amplitude of multiplicative selection bias before the analytical correction is ~2% . After the analytical bias correction, the amplitudes of multiplicative biases shown in the top panels of Figures 11 and 12 are below 0.1%, which is within the LSST DESC science requirement (|m| < 0.3%, see The LSST Dark Energy Science Collaboration et al. 2018 for details). After applying our corrections, the amplitudes of additive biases in the bottom panel of Figure 11 and 12 are below  $1 \times 10^{-4}$ . Therefore, we conclude that our analytical correction reduces the selection bias to the sub-percent level for isolated galaxies. This result is consistent with the selection bias correction with a hard selection cut on a single property, shown in Figure 5 of Li et al. (2022b).

Note that the tests above only include galaxy sample selection using one observable. We will test for shear biases due to selections combining FPFS magnitude, resolution and peak modes together in the following sections.

#### 4.1.2 Detected center

We next test the performance of our method for the galaxies detected from the isolated galaxy-image simulations where galaxies have sub-pixel offsets from the center of the postage stamps. The default setup for the soft selection is the same as in Figure 7. The results are shown in Figures 13 and 14. Note, these plots show the results as a function of cuts on one parameter; however, cuts are being made simultaneously on the other parameters. In addition, in our formalism, one galaxy can be detected several times with different centers with detection weight < 1.

Before the analytical correction for the detection bias and selection bias, the multiplicative biases are at a level of -5%. Comparing the multiplicative biases before analytical correction to those with fixed centers in Figures 11 and 12, we conclude that the detection process itself causes approximately -4% multiplicative biases for the isolated galaxy image simulations. This multiplicative bias is caused by the selection of noisy sheared pixels above a threshold, peak identification from noisy sheared pixels and setting the peaks as galaxy centroids.

After the analytical correction for noise bias, selection bias and detection bias, the multiplicative biases are less than 0.2% (with statistical error ~0.1%). Note, the multiplicative shear biases are within the LSST requirements on the control of multiplicative bias (|m| < 0.3%). The measured additive biases after our corrections are below  $1 \times 10^{-4}$ . Therefore, we conclude that our analytical correction is able to reduce the shear-estimation biases, including the bias from detection, to |m| < 0.3% for isolated galaxies.

#### 4.2 Blended galaxies

# 4.2.1 Number density

Before showing the accuracy of the algorithm on blended galaxy image simulations, we characterize the detected/selected galaxy sample in those simulations. The detected number density after the postselection step is strongly dependent on the smoothing scale of the Gaussian kernel,  $\sigma_h$ . Therefore, we test two smoothing scales, namely  $\sigma_h = 0.59$  (FWHM=1.4) and  $\sigma_h = 0.45$  (FWHM=1.1) for the image simulation with input galaxy number density of 85 arcmin<sup>-2</sup>.

For smoothing scale of  $\sigma_h = 0'.59$ , the number density of galaxies with non-zero selection weight after the postselection step is 31 arcmin<sup>-2</sup>. Since many of the galaxies are downweighted by the selection weight, we define the effective number of galaxies as

$$N_{\text{eff}} = \sum_{l=1}^{N_{\text{gal}}} w_2^{(l)}, \tag{63}$$

assuming that the unweighted ellipticity,  $e_{\alpha}$ , of each galaxy contributes equally to the shear estimation. One can divide the galaxy number by the area to get the effective number density. The galaxy number density after the postselection step is 9 arcmin<sup>-2</sup>. For smoothing scale of  $\sigma_h = 0.45$ , the number density of galaxies with non-zero selection weight is 34 arcmin<sup>-2</sup>, and the effective galaxy number density is 16 arcmin<sup>-2</sup>. Note, in this paper, we do not discuss the optimal choice for the smoothing scale,  $\sigma_h$ .

For comparison, the effective number density of the HSC shape catalog is ~20 arcmin<sup>-2</sup> (Mandelbaum et al. 2018a; Li et al. 2022a). The number density decreases as the noise variance or the PSF size increase. We note that the image noise variance in the simulations here is twice the average of the HSC survey in *i*-band; our PSF FWHM estimated with Gaussian weighted moments is 10% larger than the HSC's FWHM. In addition, the PSF model is not exactly the same as HSC PSFs. For this reason, we generally expect a lower number detected number density in these simulations than in the actual HSC shape catalog.

We find that, for isolated galaxies, the number of detections is not strongly dependent on the smoothing scale, and the differences between their shear measurement biases are consistent at the  $2\sigma$  level. Therefore, we only showed the results for  $\sigma_h = 0'.59$  for the isolated galaxy simulations. We defer a more detailed exploration of the dependence of biases and detected number density as a function of  $\sigma_h$  and other free parameters to future work.

#### 4.2.2 Shear estimation bias

We show the multiplicative and additive bias in the shear estimator with these two smoothing scales for the galaxies detected from the blended image simulations. The input galaxies number densities of the simulations are  $85 \, \mathrm{arcsec^{-2}}$ . The default setup for the soft selection is the same as in Figure 8. The results are shown in Figures 15-16.

Before the correction for the detection and selection bias, the multiplicative shear biases are at a level of -5%. Comparing the multiplicative biases before analytical correction to those for isolated galaxies with fixed center in Figures 11 and 12, we conclude that the detection process causes about -4% multiplicative biases for the blended image simulations. This amplitude of this detection bias in blended image simulation is consistent with what has been reported in Sheldon et al. (2020). We note that the uncorrected bias is similar to the uncorrected bias we found without blending. This is because FPFS does not make any assumptions regarding galaxy morphology, and blended galaxies at the same redshift can be considered as a single galaxy with a complicated morphology. However, such differences in morphology do not noticeably degrade the accuracy of our algorithm.

After the analytical corrections for noise bias, selection bias and detection bias, the multiplicative biases are below 0.6%, with statistical error of ~0.15% for the two different smoothing scales that we have tested. The measured additive biases are below  $1\times10^{-4}$  for both smoothing scales. However, we note that there is some variation in multiplicative bias within the range  $|m|<6\times10^{-3}$  for the blended image simulations. It is possible that this is caused by false detections at empty locations due to fluctuations of image noise. We will study the origin of these biases (including confirmation and mitigation of the false detection effect or other relevant effects) in detail in our future work.

We show the results for the blended image simulation with input galaxy number density of 170  ${\rm arcmin^{-2}}$  in Appendix E. The results are consistent with what we found here for the simulation with input galaxy number density of 85  ${\rm arcmin^{-2}}$ .

The simple analytical correction reduces the multiplicative bias by an order of magnitude. Although the bias reduction is not complete, it is a very important start that establishes the promise of this analytical method to eventually reach the stringent requirements of Stage IV surveys.

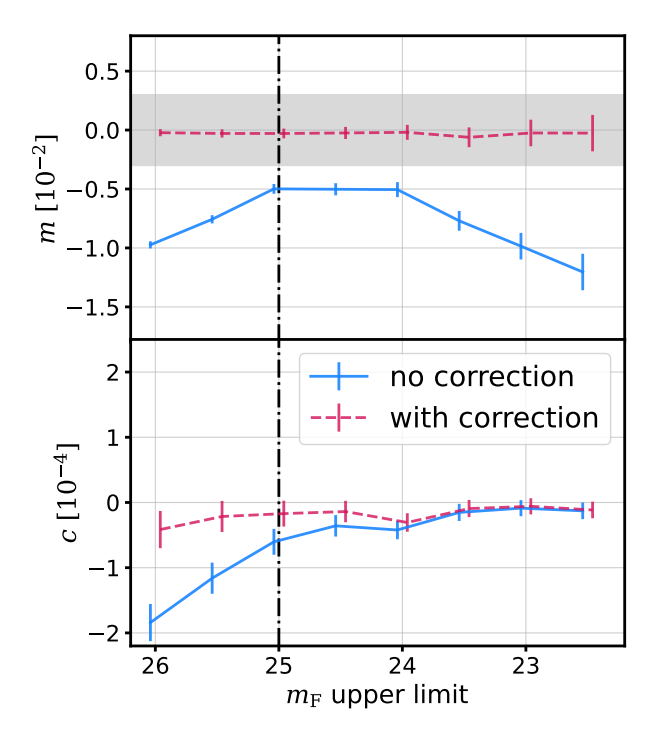


**Figure 11.** The multiplicative bias (top panel) and additive bias (bottom panel) in shear as functions of the upper limit of FPFS magnitude ( $m_{\rm F}$ ) measured from the isolated image simulation. The coordinate center for the measurement is set to the truth, so no detection process was carried out. We do not apply any cut on other observables. The solid (dashed) lines are results before (after) the correction for shear-dependent selection bias. The dark shaded region is the LSST DESC requirement on the control of multiplicative shear bias. The vertical dash-dotted line is the default cut on magnitude of the postselection.

#### 4.3 HSC Year 3

In the previous subsections, we showed the performance of our algorithm with different smoothing scales on simulations that have double the variance of HSC survey image noise. Here, we test our algorithm, setting  $\sigma_h = 0.45''$ , on images with noise variance set to the mean of the noise variance in three-year HSC (HSC-Y3) data (Li et al. 2022a), and predict the performance of the algorithm on the HSC-Y3 data.

The results for different magnitude and resolution cuts are shown as dashed lines in Figure 17 and 18, respectively. In addition, we use our auto-differentiation code (Li et al. prep) to fully correct the second-order noise bias, and the results for different magnitude and resolution cuts are shown as solid lines in Figure 17 and 18, respectively. The multiplicative bias is smaller than that in the tests with double the typical HSC noise variance, indicating that at least some of the non-zero multiplicative bias in results earlier in this paper were caused by the image noise. We also find that the multiplicative bias slightly reduces by ~0.2% after we include all of the secondorder noise bias correction terms (Li et al. prep), indicating the bias from the neglected terms was not very significant for the precision of tests in this paper. We still find a residual multiplicative bias of about -0.3% even after including all the second-order noise bias correction terms. We suspect this is due to (i) false detections; or (ii) higher-order noise bias, and we will investigate the cause of this residual bias in our future work.

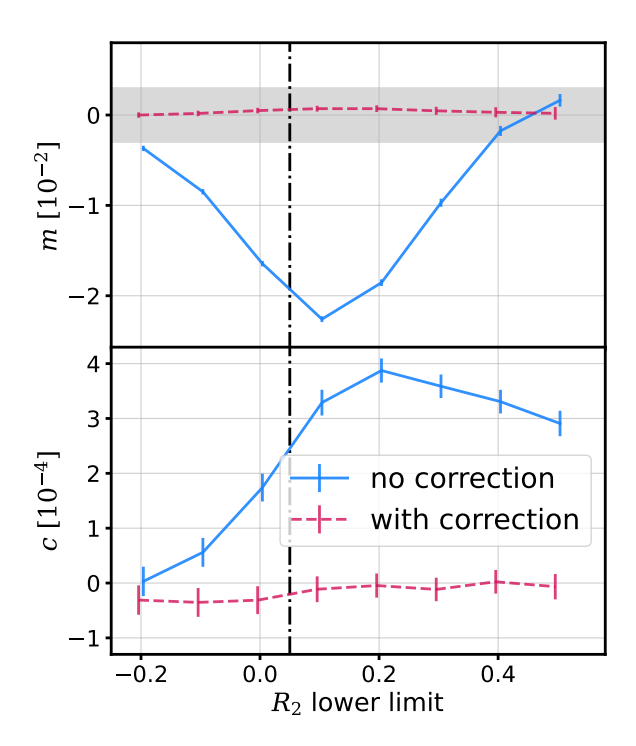


**Figure 12.** Similar to Figure (11), but here the shear estimation biases measured from the isolated image simulation are shown as functions of the lower limit of FPFS resolution ( $R_2$ ). The vertical dash-dotted line is the default cut on resolution of the postselection.

# 5 SUMMARY AND OUTLOOK

In this paper, we analytically correct for detection and selection bias in shear estimation for the FPFS shear estimator applied at the image pixel level by deriving the shear response of image pixels. We also analytically correct for the second-order noise bias in the detection process. Crucially, the analytic correction does not depend upon calibration via external galaxy image simulations. Moreover, unlike Bayesian Fourier Domain (BFD Bernstein & Armstrong 2014; Bernstein et al. 2016), our shear estimator does not require a deep reference sample; and unlike Metacalibration/Metadetection (Sheldon & Huff 2017; Huff & Mandelbaum 2017; Sheldon et al. 2020), it does not require artificial shearing of each observed galaxy image. Our publicly-available code (https://github.com/mr-superonion/FPFS) can process more than a thousand galaxy images per CPU second.

Using mock images of galaxies distorted with an input known shear, we demonstrate that our shear estimator reaches sub-percent level accuracy not only for isolated galaxies but also for blended galaxies with an extremely high galaxy number density under HSC-like observing conditions.

Future works should test the performance of this novel detector/shear estimator using more complicated simulations. Here we list the assumptions in our image simulations used to test the method in this paper, which should be the targets of the future tests:

(i) The image noise is homogeneous across the sky; however, in

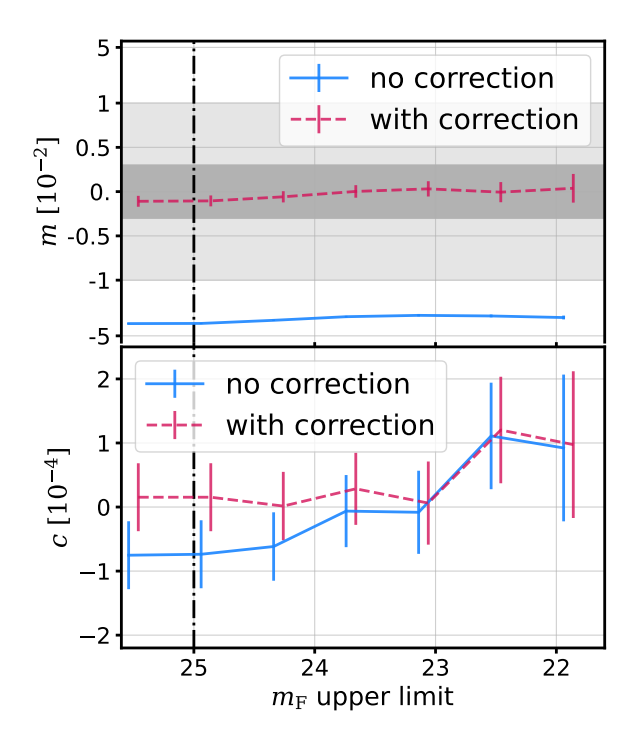


**Figure 13.** Similar to Figure (11) on the isolated image simulation, but the coordinate center for the measurement is set to the peaks identified with FPFS detector. The FPFS resolution cut is set to  $R_2 > 0.05$ . The y-axis for the light light shaded region of the top panel is in linear scale; while the other regions are in log scale. The errorbars are much smaller than the log scale so that they cannot be visualized in the log region. In addition, the smoothing scale of the Gaussian kernel,  $\sigma_h$ , is set to 0'.59. The vertical dash-dotted line is the default cut on magnitude of the postselection.

reality, galaxy photon noise and the variation of background photon noise are inhomogeneous at small scales and large scales, respectively

- (ii) The PSF is fixed rather than varying across the sky; however, in reality, the PSF is a function of the position on the focal plane of an exposure.
- (iii) Atmospheric chromatic effects on PSF modelling, e.g., wavelength dependence of seeing and atmospheric differential chromatic refraction (Meyers & Burchat 2015).
- (iv) The input shear is the same for every galaxy in the image; however, in reality, the shear is a function of galaxy redshift.
- (v) The image is well sampled; however, for spaced-based surveys, images of single exposures are not well sampled.
- (vi) Sky background, stars and image artifacts are not included in our simulations.

For the first two assumptions, we have proposed solutions in this paper: (i) we derive the formalism for inhomogeneous noise in Appendix D; and (ii) we propose a solution to PSF variation by conducting the postselection and measurement using the PSF modelled for each galaxy after the preselection using the average PSF over a field in Section 2.2.3. We will explicitly test the performance of the shear estimator with simulations that violate these two assumptions in our future work. For the last three assumptions, we will quantify their importance with realistic image simulations, and improve our algorithm once the importance of these issues is better understood.

Another thing to note is that the formalism presented here is for

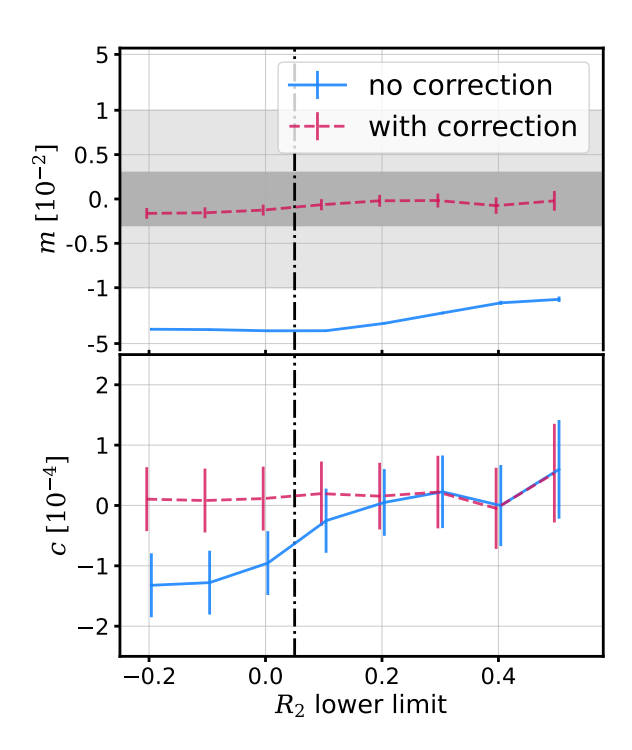


**Figure 14.** Similar to Figure (12), but here the shear estimation biases measured from the isolated image simulation are shown as functions of the lower limit of FPFS resolution ( $R_2$ ). The FPFS magnitude cut is fixed at  $m_F < 25$ . In addition, the smoothing scale of the Gaussian kernel,  $\sigma_h$ , is set to 0".59. The vertical dash-dotted line is the default cut on magnitude of the postselection.

estimation of the average shear within a patch of sky. Gatti et al. (2021) provided a consistent correction for selection bias in two-point correlation functions for Metacalibration in their Appendix A. In our future work, we will study in detail the correction for detection and selection bias when estimating two-point correlation functions using our shear estimator.

Furthermore, we will attempt to understand the residual halfpercent bias in the blended simulations and test the detailed performance of the method as a function of the choices of hyperparameters (e.g., the smoothing scales, for which we only considered two options in this work).

The future work outlined here is all in the spirit of getting this very promising approach ready for direct application to Stage-IV surveys. In addition, we are going to apply the shear estimator to the ongoing surveys (e.g., HSC) to test its performance.

# **ACKNOWLEDGEMENTS**

This work was supported by a grant from the Simons Foundation (Simons Investigator in Astrophysics, Award ID 620789).

We thank Mike Jarvis, Scott Dodelson, Arun Kannawadi, Matthew Becker, Erin Sheldon and Gary Bernstein for their useful comments on the paper.

This paper uses the parameters of the HSC SSP observational conditions. The Hyper Suprime-Cam (HSC) collaboration includes

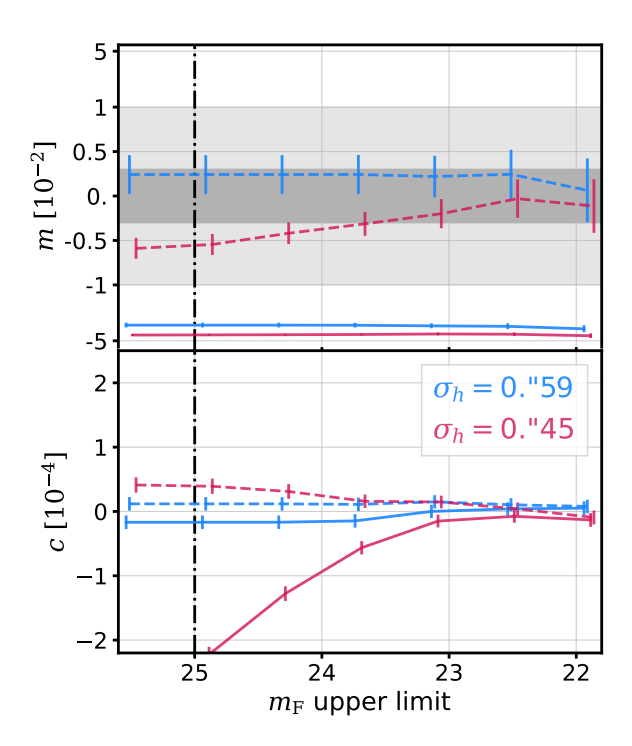


**Figure 15.** Similar to Figure (13), but measured from the blended galaxy image simulation with number density 85 arcmin<sup>-2</sup> with two smoothing scales: 0'.59 (blue) and 0'.45 (red). The solid (dashed) lines are results before (after) the correction for shear-dependent detection bias and selection bias. The vertical dash-dotted line is the default cut on magnitude of the postselection.

the astronomical communities of Japan and Taiwan, and Princeton University. The HSC instrumentation and software were developed by the National Astronomical Observatory of Japan (NAOJ), the Kavli Institute for the Physics and Mathematics of the Universe (Kavli IPMU), the University of Tokyo, the High Energy Accelerator Research Organization (KEK), the Academia Sinica Institute for Astronomy and Astrophysics in Taiwan (ASIAA), and Princeton University. Funding was contributed by the FIRST program from Japanese Cabinet Office, the Ministry of Education, Culture, Sports, Science and Technology (MEXT), the Japan Society for the Promotion of Science (JSPS), Japan Science and Technology Agency (JST), the Toray Science Foundation, NAOJ, Kavli IPMU, KEK, ASIAA, and Princeton University.

This paper makes use of software developed for the Vera C. Rubin Observatory. We thank the Vera C. Rubin Observatory for making their code available as free software at http://dm.lsst.org.

We thank the maintainers of numpy (Harris et al. 2020), scipy (Virtanen et al. 2020), numba (Lam et al. 2015), Matplotlib (Hunter 2007), GalSim (Rowe et al. 2015) for their excellent open-source software.

# DATA AVAILABILITY

The code used for image processing and galaxy image simulation in this paper is available from https://github.com/mr-superonion/FPFS/tree/v3.0.2.

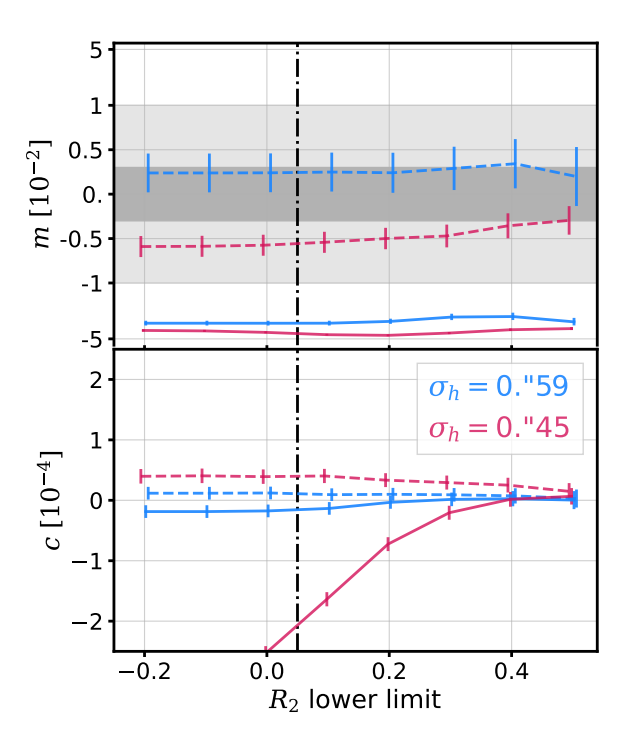


**Figure 16.** Similar to Figure (14), but measured from the blended galaxy image simulation with number density 85 arcmin<sup>-2</sup> with two smoothing scales: 0'.'59 (blue) and 0'.'45 (red). The solid (dashed) lines are results before (after) the correction for shear-dependent detection bias and selection bias. The vertical dash-dotted line is the default cut on magnitude of the postselection.

#### REFERENCES

Li X., Zhang J., 2016, ApJ, 830, 116

Li H., Zhang J., 2021, ApJ, 911, 115

Li X., et al., 2022a, PASJ, 74, 421

```
Bartelmann M., Schneider P., 2001, Physics Reports, 340, 291
Becker M. R., Sheldon E. S., in prep.
Bernstein G. M., 2010, MNRAS, 406, 2793
Bernstein G. M., Armstrong R., 2014, MNRAS, 438, 1880
Bernstein G. M., Jarvis M., 2002, AJ, 123, 583
Bernstein G. M., Armstrong R., Krawiec C., March M. C., 2016, MNRAS,
    459, 4467
Bosch J., et al., 2018, PASJ, 70, S5
Eckert K., et al., 2020, MNRAS, 497, 2529
Gatti M., et al., 2021, MNRAS, 504, 4312
Givans J. J., et al., 2022, PASP, 134, 014001
Harris C. R., et al., 2020, Nature, 585, 357
Heymans C., et al., 2006, MNRAS, 368, 1323
Hirata C., Seljak U., 2003, MNRAS, 343, 459
Huff E., Mandelbaum R., 2017, preprint, (arXiv: 1702.02600)
Hunter J. D., 2007, Computing in Science and Engineering, 9, 90
Huterer D., Takada M., Bernstein G., Jain B., 2006, MNRAS, 366, 101
Ivezić Ž., et al., 2019, ApJ, 873, 111
Kaiser N., 2000, The Astrophysical Journal, 537, 555
Kilbinger M., 2015, Reports on Progress in Physics, 78, 086901
Lam S. K., Pitrou A., Seibert S., 2015, in Proceedings of the Sec-
   ond Workshop on the LLVM Compiler Infrastructure in HPC.
   LLVM '15. Association for Computing Machinery, New York, NY,
   USA, doi:10.1145/2833157.2833162, https://doi.org/10.1145/
    2833157.2833162
Laureijs R., et al., 2011, preprint, (arXiv:1110.3193)
```

Li X., Katayama N., Oguri M., More S., 2018, MNRAS, 481, 4445

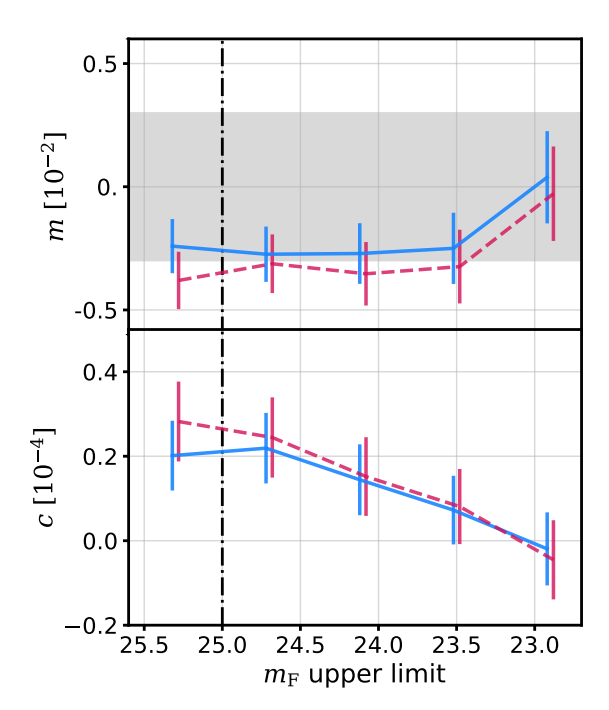


**Figure 17.** Similar to Figure (15), but measured from the blended galaxy image simulation with the average noise level of the HSC three-year data (Li et al. 2022a). The solid lines include all the nosie bias correction term using auto-diff; whereas the dashed lines only include the noise bias correction terms given out in this paper. Shaded region is for LSST ten-year requirement on the control of multiplicative bias.

```
Li X., Li Y., Massey R., 2022b, MNRAS, 511, 4850
Li X., et al., in prep.
MacCrann N., et al., 2022, MNRAS, 509, 3371
Mandelbaum R., 2018, ARA&A, 56, 393
Mandelbaum R., Lackner C., Leauthaud A., Rowe B., 2012, COSMOS real
    galaxy dataset, doi:10.5281/zenodo.3242143, https://doi.org/10.
    5281/zenodo.3242143
Mandelbaum R., et al., 2014, ApJS, 212, 5
Mandelbaum R., et al., 2018a, PASJ, 70, S25
Mandelbaum R., et al., 2018b, MNRAS, 481, 3170
Massey R., Refregier A., 2005, MNRAS, 363, 197
Massey R., et al., 2007, MNRAS, 376, 13
Massey R., Kitching T., Richard J., 2010, Reports on Progress in Physics, 73,
   086901
Massey R., et al., 2013, MNRAS, 429, 661
Meyers J. E., Burchat P. R., 2015, ApJ, 807, 182
Moffat A. F. J., 1969, A&A, 3, 455
Pujol A., Kilbinger M., Sureau F., Bobin J., 2019, A&A, 621, A2
Refregier A., 2003, MNRAS, 338, 35
Refregier A., Kacprzak T., Amara A., Bridle S., Rowe B., 2012, MNRAS,
Rowe B. T. P., et al., 2015, Astronomy and Computing, 10, 121
Sérsic J. L., 1963, Boletin de la Asociacion Argentina de Astronomia La
    Plata Argentina, 6, 41
Sheldon E. S., Huff E. M., 2017, ApJ, 841, 24
Sheldon E. S., Becker M. R., MacCrann N., Jarvis M., 2020, ApJ, 902, 138
```

The LSST Dark Energy Science Collaboration et al., 2018, arXiv e-prints, p.

Spergel D., et al., 2015, preprint, (arXiv:1503.03757)

Virtanen P., et al., 2020, Nature Methods, 17, 261

Zhang J., Luo W., Foucaud S., 2015, JCAP, 1, 24

arXiv:1809.01669

Zhang J., 2008, MNRAS, 383, 113

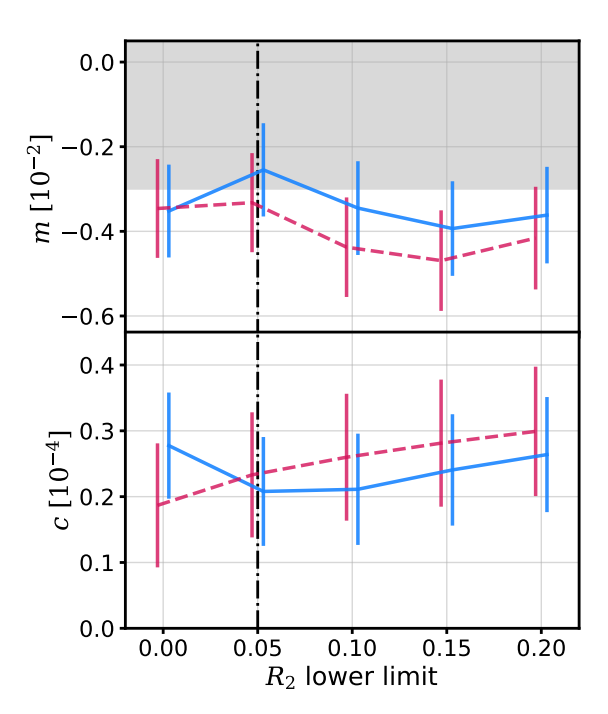


**Figure 18.** Similar to Figure (16), but measured from the blended galaxy image simulation with the average noise level of the HSC three-year data (Li et al. 2022a). The solid lines include all the nosie bias correction term using auto-diff; whereas the dashed lines only include the noise bias correction terms given out in this paper. Shaded region is for LSST ten-year requirement on the control of multiplicative bias.

Zhang J., Zhang P., Luo W., 2017, ApJ, 834, 8 de Vaucouleurs G., 1948, Annales d'Astrophysique, 11, 247

## APPENDIX A: SHEAR PERTURBATION

We use noiseless isolated galaxy image simulations (as demonstrated in the left panel of Figure 6) to confirm the second-order shear bias residual is consistent with zero (as shown in equation (4)) when galaxies are isotropically oriented. Moreover, we determine the coefficient before the neglected third-order term in shear in equation (4), which corresponds to a contribution to the multiplicative bias that is second-order in shear. The multiplicative biases for different galaxy samples are shown in Figure B1. The coefficient, which depends on galaxy properties, is approximately -0.20 for galaxies with FPFS magnitude brighter than 25.5, and -0.13 for galaxies with FPFS magnitude brighter than 24.9. We note that this third-order shear estimation bias needs to be calibrated with external image simulation for shear estimation in the intermediate-shear regime.

# APPENDIX B: SPIN NUMBER AND ROTATION SYMMETRY

In this appendix, we discuss the connection between the spin number of galaxy properties and the rotation symmetry. Furthermore, we derive the spin number of the product of two properties. These concepts will be used to explain equation (4), but are also relevant to some of the other equations in this work.

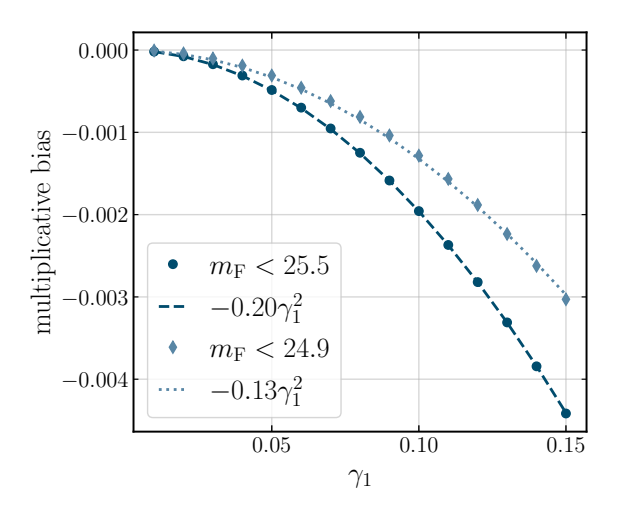


**Figure B1.** Multiplicative bias as a function of input shear with two different FPFS magnitude cuts. The circles (diamonds) denote the multiplicative bias in galaxy sample with magnitude brighter than 25.5 (24.9). The biases scale as  $-0.20\gamma_1^2$  and  $-0.13\gamma_1^2$ , respectively.

The spin number of an observable that is measured from the image coordinate system x describes how the observable transforms when the coordinate system, x, rotates. The reference coordinate system is set to the two-dimensional sky coordinates adopting the flat-sky approximation with +x being the horizontal axis to the west; +y being the vertical axis to the north.

Here we focus on properties that only have one spin component. In a specific two-dimensional image coordinate system, which is a rotated, dilated and/or weighted transform of the reference coordinates, the representation of an observable can be written as a complex number:

$$v_x = v_{x1} + iv_{x2}, (B1)$$

where  $v_{x1}$  and  $v_{x2}$  are two components of the observable. These components are

$$v_{x1} = \frac{v_x + v_x^*}{2},$$

$$v_{x2} = \frac{v_x - v_x^*}{2i},$$
(B2)

where  $x^*$  refers to the complex conjugate of x. Note,  $v_x$  is not a field at the position x; rather, it is the projection of an observable onto the image coordinate system, x. If the image coordinate system x changes (e.g., through a rotation, flip or dilation), the representation of the observable in the image coordinates also changes:  $v_x \longrightarrow v_{x'}$ , since the measurement is conducted in the transformed coordinates. Note, the observable itself does not change when the image coordinate system transforms, but its representation with respect to the image coordinate system does change.

In this appendix, we focus on the rotation transform. The representation of a spin-m observable with respect to an image coordinate system x can be written as

$$v_x = v \exp\left(im(\theta_0 - \theta)\right) \,. \tag{B3}$$

v is the amplitude of the observable,  $\theta_0$  is the direction of the observable with respect to the main axis of the reference coordinate system, and  $\theta$  is the direction of the main axis of the image coordinate system with respect to the reference coordinate system. Now

we have

$$v_{x1} = v \cos(m(\theta_0 - \theta)),$$
  

$$v_{x2} = v \sin(m(\theta_0 - \theta)).$$
(B4)

By definition, the representation of a spin-m ( $m \neq 0$ ) observable is negated when the coordinate system rotates by  $\pi/|m|$ :  $\theta \to \theta + \pi/|m|$ . As a result, when the coordinate system rotates by an odd multiple of  $\frac{\pi}{|m|}$ , the representation negates; when the coordinate system rotates by an even multiple of  $\frac{\pi}{|m|}$ , the representation transforms back to its original value. For the case m=0, the representation of the observable does not change when the coordinate system rotates.

Since equation (4) involves products of quantities with different spins, in order to study equation (4) in detail, we determine the spin number of the product of two properties measured on the same coordinate system. We use  $v_x$  for the first observable, and the second observable is denoted as

$$v_x' = v' \exp\left(im'(\theta_0' - \theta)\right). \tag{B5}$$

Since these two properties are measured in the same image coordinate,  $\theta$  is the same as the one in equation (B3). The products of these two properties and their complex conjugates are

$$v_{x}^{*}v_{x}' = v'v \exp\left(-i(m'-m)\theta + m'\theta_{0}' - m\theta_{0})\right), v_{x}v_{x}' = v'v \exp\left(-i(m'+m)\theta + m'\theta_{0}' + m\theta_{0})\right).$$
(B6)

These equations tell how the representations of products transform as the coordinate system rotates as  $\theta \to \theta + \Delta \theta$ . We conclude that the products are combinations of spin-(m+m') and spin-(m-m') quantities. The terms  $m'\theta'_0 \pm m\theta_0$  determine the angular phase of the products with respect to the reference coordinates, which does not change as the image coordinates rotate since the observable itself does not rotate with the coordinates. According to equation (B2), the products between the components of these two representations can only be spin-(m+m') or spin-(m-m') since they can be written as linear combinations of  $v_*^*v_r'$  and  $v_*v_r'$ .

Some observables can be decomposed into many spin components; however, the weak lensing shear,  $\gamma_1 + i\gamma_2$ , is a pure spin-2 quantity according to the definition shear field (Bartelmann & Schneider 2001):

$$\gamma(x,y) \propto \left(\frac{\partial^2}{\partial x^2} - \frac{\partial^2}{\partial y^2}\right) \Phi(x,y) + 2i \frac{\partial}{\partial x} \frac{\partial}{\partial y} \Phi(x,y),$$
(B7)

where  $\Phi$  is a scalar field defined on the sky coordinates. In the vector space centered at a point (x,y),  $\gamma$  is a spin-2 vector since  $(\frac{\partial^2}{\partial x^2} - \frac{\partial^2}{\partial y^2})$ ,  $(\frac{\partial^2}{\partial x^2})$  negates when the coordinates of the vector space rotate by  $\pi/2$  (while keeping the coordinates center the same). In order to measure shear with the FPFS ellipticity, we define it as a pure spin-2 quantity. In addition, we require the ellipticity to not have an angular phase offset with respect to shear after averaging over a large number of galaxies, namely  $\theta_0^{(e)} = \theta_0^{(e)} = \theta_0$  for both shear and ellipticity.

We take a closer look at equation (4) at the single galaxy level and keep the perturbation terms up to the second order in shear:

$$we_{\alpha} = \bar{w}\bar{e}_{\alpha} + \left. \frac{\partial(we_{\alpha})}{\partial \gamma_{\mu}} \right|_{\gamma_{\mu}=0} \gamma_{\mu} + \left. \frac{\partial^{2}(we_{\alpha})}{\partial \gamma_{\mu}\partial \gamma_{\nu}} \right|_{\gamma_{\mu,\nu}=0} \gamma_{\mu}\gamma_{\nu} + O\left(\gamma_{\alpha}^{3}\right), \quad (B8)$$

where we adopt Einstein summation notation. Since all the derivatives are evaluated at zero shear, we neglect the  $|_{\gamma_{\mu}=0}$  in the following discussion. Assuming that the selection weight is spin-0, the left-hand side is a spin-2 observable. Since the equation should be valid on image coordinates with any arbitrary orientation, each term on the right-hand-side with different orders in shear should be spin-2. In addition, the expectation of each term and  $\langle e_{\alpha} \rangle$  should have the

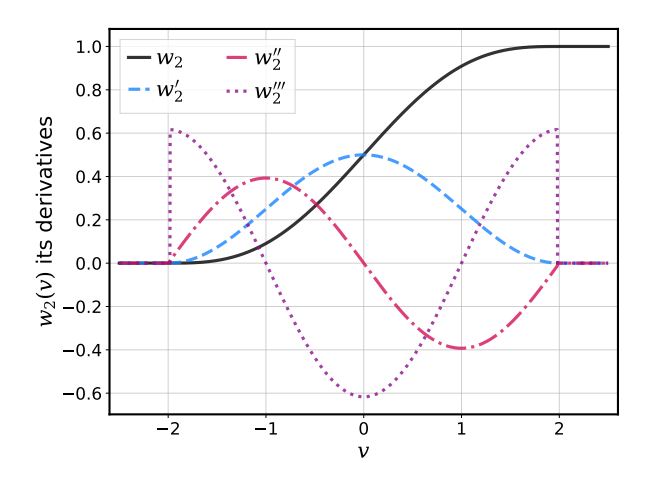


**Figure C1.** Solid line is the truncated sine selection function,  $w_2$  (defined in equation (46)). The dashed, dotted-dash and dotted lines are its first, second and third-order derivatives, respectively.

same angular phase with respect to the reference coordinate system. We will discuss the first-order and second-order terms in shear, separately.

First, we look into the term that is first order in shear:  $\frac{\partial (we_\alpha)}{\partial \gamma_\mu} \gamma_\mu$  ( $\alpha, \mu \in \{1, 2\}$ ). Since  $\gamma_\mu$  is spin-2, any non-zero contribution from  $\frac{\partial (we_\alpha)}{\partial \gamma_\mu}$  must be a combination of spin-0 and spin-4 properties, as we require their product to be spin-2. The diagonal elements of the shear response matrix are composed of spin-0 and spin-4 quantities; whereas, the off-diagonal elements of the shear response matrix,  $\frac{\partial (we_\mu)}{\partial \gamma_\nu}$  ( $\mu \neq \nu$ ), cannot be spin-0, since the angular phases of  $\langle e_\mu \rangle$  and  $\gamma_\nu$  differ by  $\pi/4$ . Therefore, the off-diagonal terms of the shear response matrix can only be spin-4. In summary, the expectation values of the diagonal terms are nonzero, because they are the expectations of spin-0 and spin-4 properties of intrinsic galaxies, and the former is nonzero even for intrinsic (unlensed) properties. In contrast, the off-diagonal terms have an expectation value of zero and do not contribute to equation (4), since they are expectation values of spin-4 properties of intrinsic galaxies.

Then we focus on the term that is second order in shear:  $\frac{\partial^2(we_a)}{\partial \gamma_\mu \partial \gamma_\nu} \gamma_\mu \gamma_\nu$  ( $\alpha, \mu, \nu \in \{1,2\}$ ). According to the rule for spin number of products,  $\gamma_\mu \gamma_\nu$  is a combination of spin-0 and spin-4 properties of intrinsic galaxies. Therefore, any non-zero contributions from  $\frac{\partial^2(we_a)}{\partial \gamma_\mu \partial \gamma_\nu}$  must be a combination of spin-2 and spin-6 properties, as we require the product to be spin-2. The expectation values of these spin-2 and spin-6 properties of intrinsic galaxies are identically zero (assumption 1), and do not contribute to equation (4).

#### APPENDIX C: NOISE BIAS CORRECTION

In this appendix, we focus on the Hessian matrix in equation (9),  $\frac{\partial^2(\bar{w}\bar{e}_{\sigma})}{\partial v_i \partial v_j}$ , which can be expanded to

$$\frac{\partial^{2}(\tilde{w}\tilde{e}_{\alpha})}{\partial v_{i}\partial v_{i}} = \tilde{w}\frac{\partial^{2}\tilde{e}_{\alpha}}{\partial v_{i}\partial v_{i}} + \frac{\partial \tilde{w}}{\partial v_{i}}\frac{\partial \tilde{e}_{\alpha}}{\partial v_{i}} + \frac{\partial \tilde{w}}{\partial v_{i}}\frac{\partial \tilde{e}_{\alpha}}{\partial v_{i}} + \tilde{e}_{\alpha}\frac{\partial^{2}\tilde{w}_{\alpha}}{\partial v_{i}\partial v_{i}}, \tag{C1}$$

following the product rule for derivatives. Since the covariance matrix in equation (9),  $K_{v_i}^{v_j}$ , is by definition symmetric, the noise bias

correction term for the average of the weighted ellipticity is

$$\Delta \langle \tilde{w}\tilde{e}_{\alpha} \rangle_{\text{noise}} = \frac{1}{2} \left\langle \tilde{w} \frac{\partial^{2} \tilde{e}_{\alpha}}{\partial v_{i} \partial v_{j}} K_{v_{i}}^{v_{j}} + 2 \frac{\partial \tilde{w}}{\partial v_{i}} \frac{\partial \tilde{e}_{\alpha}}{\partial v_{j}} K_{v_{i}}^{v_{j}} + \tilde{e}_{\alpha} \frac{\partial^{2} \tilde{w}}{\partial v_{i} \partial v_{j}} K_{v_{i}}^{v_{j}} \right\rangle, \tag{C2}$$

where we adopt Einstein notation on indices (i,j) throughout this appendix: repeated indices i and indices j indicate summation. In addition to the weighted ellipticity, photon noise also biases the estimation of its shear response due to the nonlinearity in the shear response. We correct for noise biases in the shear response, namely  $\langle \tilde{w} \, \tilde{e}_{\alpha;\alpha} \rangle + \langle \tilde{w}_{;\alpha} \, \tilde{e}_{\alpha} \rangle$  to accurately measure the shear response. These corrections are composed of

$$\Delta \langle \tilde{w}\tilde{e}_{\alpha;\alpha} \rangle_{\text{noise}} = \frac{1}{2} \left\langle \tilde{w} \frac{\partial^2 \tilde{e}_{\alpha;\alpha}}{\partial v_i \partial v_j} K_{v_i}^{v_j} + 2 \frac{\partial \tilde{w}}{\partial v_i} \frac{\partial \tilde{e}_{\alpha;\alpha}}{\partial v_j} K_{v_i}^{v_j} \right\rangle + \frac{1}{2} \left\langle \tilde{e}_{\alpha;\alpha} \frac{\partial^2 \tilde{w}}{\partial v_i \partial v_j} K_{v_i}^{v_j} \right\rangle$$
(C3)

and

$$\Delta \langle \tilde{w}_{;\alpha} \tilde{e}_{\alpha} \rangle_{\text{noise}} = \frac{1}{2} \left\langle \frac{\partial \tilde{w}}{\partial v_{k}} \frac{\partial^{2} \left( \tilde{v}_{k;\alpha} \tilde{e}_{\alpha} \right)}{\partial v_{i} \partial v_{j}} K_{v_{i}}^{v_{j}} + 2 \frac{\partial^{2} \tilde{w}}{\partial v_{k} \partial v_{i}} \frac{\partial \left( \tilde{v}_{k;\alpha} \tilde{e}_{\alpha} \right)}{\partial v_{j}} K_{v_{i}}^{v_{j}} \right\rangle 
+ \frac{1}{2} \left\langle \tilde{v}_{k;\alpha} \tilde{e}_{\alpha} \frac{\partial^{3} \tilde{w}}{\partial v_{k} \partial v_{i} \partial v_{j}} K_{v_{i}}^{v_{j}} \right\rangle.$$
(C4)

Finally, the shear transform equation of the expectation value of the *noisy* weighted ellipticity is

$$\langle \tilde{w}\tilde{e}_{\alpha} \rangle - \Delta \langle \tilde{w}\tilde{e}_{\alpha} \rangle_{\text{noise}} = \gamma_{\alpha} \left( \langle \tilde{w}_{;\alpha}\tilde{e}_{\alpha} \rangle + \langle \tilde{w}\tilde{e}_{\alpha;\alpha} \rangle \right) - \gamma_{\alpha} \left( \Delta \langle \tilde{w}_{;\alpha}\tilde{e}_{\alpha} \rangle_{\text{noise}} + \Delta \langle \tilde{w}\tilde{e}_{\alpha;\alpha} \rangle_{\text{noise}} \right) + O\left( \gamma_{\alpha}^{3} \right) + O\left( (\delta v)^{4} \right)$$
(C5)

Here we separate the noise bias correction terms defined in equations (C2)–(C4) into terms that only include zeroth, first and higher-order derivatives of the selection weight function with respect to the basis modes.

#### C1 Zeroth-order terms

The correction terms only including the zeroth-order derivative of selection weight function are

$$\tilde{w} \left\{ \frac{\partial^2 \tilde{e}_{\alpha}}{2 \, \partial v_i \partial v_j} K_{v_i}^{v_j} \right\}$$
 and  $\tilde{w} \left\{ \frac{\partial^2 \tilde{e}_{\alpha;\alpha}}{2 \, \partial v_i \partial v_j} K_{v_i}^{v_j} \right\}$ .

The terms in the bracket are the second-order corrections for the noise biases in ellipticity and its shear response. These noise bias corrections have been presented in equations (21), (A1) and (A2) of Li et al. (2022b).

It is worth pointing out that the notation in Li et al. (2022b) is slightly different from the above, and we translate these equations here. We can derive the correction term from equation (21) of Li et al. (2022b):

$$\begin{split} \frac{\partial^2 \tilde{e}_1}{2 \, \partial v_i \partial v_j} K_{v_i}^{v_j} &= e_1 \frac{K_{M_{00}}^{M_{00}}}{(M_{00} + C)^2} - \frac{K_{M_{22c}}^{M_{00}}}{(M_{00} + C)^2}, \\ \frac{\partial^2 \tilde{e}_2}{2 \, \partial v_i \partial v_j} K_{v_i}^{v_j} &= e_2 \frac{K_{M_{00}}^{M_{00}}}{(M_{00} + C)^2} - \frac{K_{M_{22s}}^{M_{00}}}{(M_{00} + C)^2} \end{split}$$
 (C6)

The shear response is composed of the following terms:  $s_0$ ,  $s_4$  and  $(e_\alpha)^2$ . We can derive the second-order noise bias correction terms

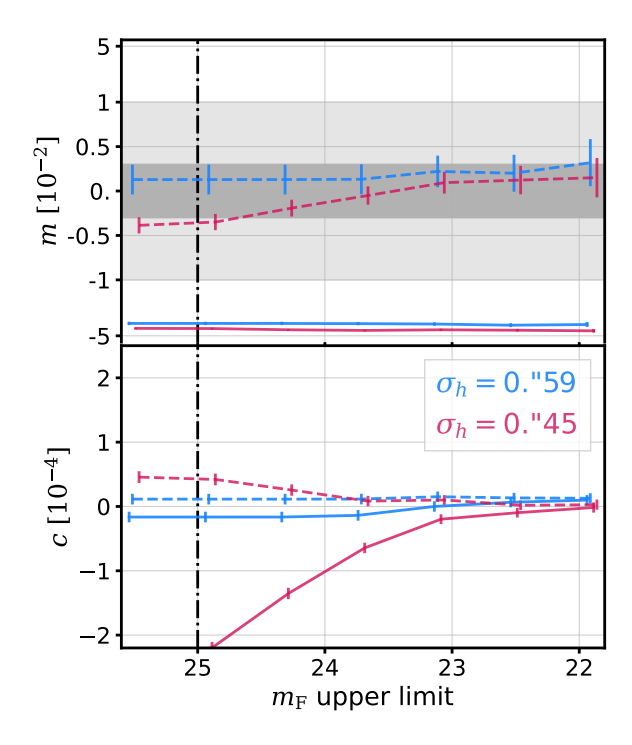


**Figure C2.** Similar to Figure (15), but measured from blended galaxy image simulation with number density 170 arcmin<sup>-2</sup>. The vertical dash-dotted line is the default cut on magnitude of the postselection.

for them, which is similar to equations (A1) and (A2) of Li et al. (2022b):

$$\begin{split} \frac{\partial^2 \tilde{s}_0}{2 \, \partial v_i \partial v_j} K_{v_i}^{v_j} &= s_0 \frac{K_{M_{00}}^{M_{00}}}{(M_{00} + C)^2} - \frac{K_{M_{00}}^{M_{00}}}{(M_{00} + C)^2}, \\ \frac{\partial^2 \tilde{s}_4}{2 \, \partial v_i \partial v_j} K_{v_i}^{v_j} &= s_4 \frac{K_{M_{00}}^{M_{00}}}{(M_{00} + C)^2} - \frac{K_{M_{00}}^{M_{40}}}{(M_{00} + C)^2}, \\ \frac{\partial^2 (\tilde{e}_1)^2}{2 \, \partial v_i \partial v_j} K_{v_i}^{v_j} &= 3 \frac{K_{M_{00}}^{M_{00}}}{(M_{00} + C)^2} + \frac{K_{M_{22c}}^{M_{22c}}}{(M_{00} + C)^2} - 4e_1 \frac{K_{M_{22c}}^{M_{00}}}{(M_{00} + C)^2}, \\ \frac{\partial^2 (\tilde{e}_2)^2}{2 \, \partial v_i \partial v_j} K_{v_i}^{v_j} &= 3 \frac{K_{M_{00}}^{M_{00}}}{(M_{00} + C)^2} + \frac{K_{M_{22s}}^{M_{22s}}}{(M_{00} + C)^2} - 4e_2 \frac{K_{M_{22s}}^{M_{00}}}{(M_{00} + C)^2}. \end{split}$$

# C2 First-order terms

Three terms include the first-order derivative of the selection weight with respect to the basis modes:

$$\frac{\partial \tilde{w}}{\partial v_k} \left\{ \frac{\partial^2 (\tilde{v}_{k;\alpha} \tilde{e}_{\alpha})}{2 \partial v_i \partial v_j} K_{v_i}^{v_j} \right\}, \tag{C8}$$

$$\frac{\partial \tilde{w}}{\partial v_i} \frac{\partial \tilde{e}_{\alpha}}{\partial v_j} K_{v_i}^{v_j} . \quad \text{and} \quad \frac{\partial \tilde{w}}{\partial v_i} \frac{\partial \tilde{e}_{\alpha;\alpha}}{\partial v_j} K_{v_i}^{v_j}$$
 (C9)

The term in the bracket of equation (C8) is the second-order noise bias correction for  $\tilde{v}_{k;\alpha}\tilde{e}_{\alpha}$ . Specifically for our shear estimation, we are using peak modes  $(q_k)$  for detection and shapelets modes  $(M_{00})$  and  $M_{20}$  for galaxy selection. The shear responses of peak modes are  $q_{k;1}$  and  $q_{k;2}$ ; and the shear responses of shapelet modes,  $M_{00}$   $(M_{20})$  are composed of  $M_{22c}$  and  $M_{22s}$   $(M_{42c}$  and  $M_{42s})$ , as shown in equations (31) ((34)). Keeping the second-order terms in the noise bias contributions, the relationships between the expectation values

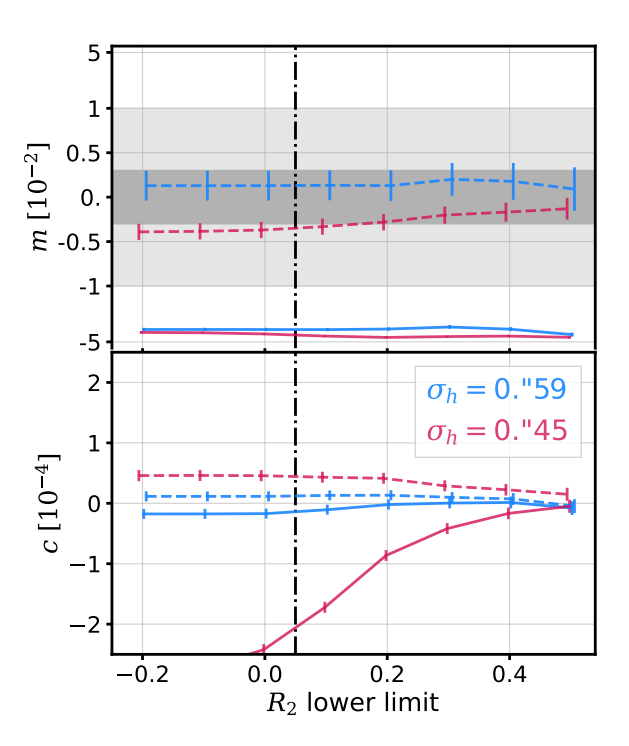


**Figure C3.** Similar to Figure (16), but measured from blended galaxy image simulation with number density 170 arcmin<sup>-2</sup>. The vertical dash-dotted line is the default cut on magnitude of the postselection.

of the noisy observables (e.g.,  $\tilde{e}_1\tilde{q}_{k;1}$ ,  $\tilde{e}_1\tilde{M}_{22c}$ ,  $\tilde{e}_1\tilde{M}_{42c}$ ) and the noiseless correspondents are derived using the Hessian matrix and the covariance matrix in equation (C8):

$$\begin{split} \langle \tilde{e}_{1} \tilde{q}_{k;1} \rangle &= \left\langle e_{1} q_{k;1} \left( 1 + \frac{K_{M_{00}}^{M_{00}}}{D^{2}} \right) \right\rangle - \left\langle \frac{q_{k;1} K_{M_{00}}^{M_{22c}}}{D^{2}} \right\rangle - \left\langle \frac{e_{1} K_{M_{00}}^{q_{k;1}}}{D} \right\rangle \\ &+ \left\langle \frac{K_{M_{22c}}^{q_{k;1}}}{D} \right\rangle \,, \\ \langle \tilde{e}_{1} \tilde{M}_{22c} \rangle &= \left\langle e_{1} M_{22c} \left( 1 + \frac{K_{M_{00}}^{M_{00}}}{D^{2}} \right) - 2 \frac{e_{1} K_{M_{00}}^{M_{22c}}}{D} \right\rangle + \left\langle \frac{K_{M_{22c}}^{M_{22c}}}{D} \right\rangle \,, \\ \langle \tilde{e}_{1} \tilde{M}_{42c} \rangle &= \left\langle e_{1} M_{42c} \left( 1 + \frac{K_{M_{00}}^{M_{00}}}{D^{2}} \right) \right\rangle - \left\langle \frac{\epsilon_{1} K_{M_{00}}^{M_{22c}}}{D} \right\rangle - \left\langle \frac{e_{1} K_{M_{00}}^{M_{42c}}}{D} \right\rangle \\ &+ \left\langle \frac{K_{M_{22c}}^{M_{42c}}}{D} \right\rangle \,, \end{split}$$

where  $D = M_{00} + C$ . We only take the terms related to the first component of ellipticity as an example, and the terms for the second component have a similar form.

Next we provide the noise bias correction for the first term in equation (C9) using the derivatives of ellipticity and selection weight:

$$\left(\frac{\partial \tilde{w}}{\partial v_{i}} \frac{\partial \tilde{e}_{1}}{\partial v_{j}} K_{v_{i}}^{v_{j}}\right) = \left(\frac{\partial \tilde{w}}{\partial v_{i}} \frac{K_{v_{i}}^{M_{22c}}}{D} - \frac{\partial \tilde{w}}{\partial v_{i}} \frac{e_{1} K_{v_{i}}^{M_{00}}}{D}\right), 
\left(\frac{\partial \tilde{w}}{\partial v_{i}} \frac{\partial \tilde{e}_{2}}{\partial v_{j}} K_{v_{i}}^{v_{j}}\right) = \left(\frac{\partial \tilde{w}}{\partial v_{i}} \frac{K_{v_{i}}^{M_{22c}}}{D} - \frac{\partial \tilde{w}}{\partial v_{i}} \frac{e_{2} K_{v_{i}}^{M_{00}}}{D}\right).$$
(C11)

Also, the noise bias correction for the second term in equation (C9), using the derivatives of shear response and selection weight, is as

follows:

$$\left\langle \frac{\partial \tilde{w}}{\partial v_{i}} \frac{\partial \tilde{e}_{1;1}}{\partial v_{j}} K_{v_{i}}^{V_{j}} \right\rangle = \frac{1}{\sqrt{2}} \left\langle \frac{\partial \tilde{w}}{\partial v_{i}} \frac{K_{v_{i}}^{M_{00}}}{D} \left( \frac{C}{D} + s_{4} - 4e_{1}^{2} \right) \right\rangle 
+ \frac{4}{\sqrt{2}} \left\langle \frac{\partial \tilde{w}}{\partial v_{i}} \frac{e_{1} K_{v_{i}}^{M_{22c}}}{D} \right\rangle - \frac{1}{\sqrt{2}} \left\langle \frac{\partial \tilde{w}}{\partial v_{i}} \frac{K_{v_{i}}^{M_{40}}}{D} \right\rangle, 
\left\langle \frac{\partial \tilde{w}}{\partial v_{i}} \frac{\partial \tilde{e}_{2;2}}{\partial v_{j}} K_{v_{i}}^{V_{j}} \right\rangle = \frac{1}{\sqrt{2}} \left\langle \frac{\partial \tilde{w}}{\partial v_{i}} \frac{K_{v_{i}}^{M_{00}}}{D} \left( \frac{C}{D} + s_{4} - 4e_{2}^{2} \right) \right\rangle 
+ \frac{4}{\sqrt{2}} \left\langle \frac{\partial \tilde{w}}{\partial v_{i}} \frac{e_{2} K_{v_{i}}^{M_{22s}}}{D} \right\rangle - \frac{1}{\sqrt{2}} \left\langle \frac{\partial \tilde{w}}{\partial v_{i}} \frac{K_{v_{i}}^{M_{40}}}{D} \right\rangle.$$
(C12)

In equations (C11) and (C12),  $v_i$  can be any basis modes used for detection and selection (e.g.,  $M_{00}$ ,  $M_{40}$ ,  $q_{0...7}$ ).

# C3 Other terms

We neglect the second-order noise bias terms other than those in Appendices C1 and C2. In Li et al. (prep), we develop a pipeline to automatically derive the full second-order noise bias correction using auto-differentiation in jax. As shown in Figures 17 and 18, the multiplicative shear bias from neglecting the other terms is about 0.2%.

#### APPENDIX D: INHOMOGENEOUS NOISE

In this appendix, we focus on noise on single exposures of spacebased observations (e.g., Euclid and Roman): photon noise and read noise are not correlated over pixels on single exposures, but spacebased images are dominated by photon noise from galaxies, which is *not homogeneous* at galaxy scale.

Since image noise on single exposures is not correlated between pixels, the off-diagonal terms of the covariance matrix are zero. The covariance matrix is

$$\langle n_x n_{x'}^* \rangle = (f_x + B_x) \, \delta_{\mathcal{D}}(x - x') \,, \tag{D1}$$

where  $(f_x + B_x)$  is the spectrum of the noise covariance matrix in configuration space;  $f_x$  is the inhomogeneous surface density field of the galaxies; and  $B_x$  is the homogeneous noise variance from sky background and read noise. Since the covariance of the pixel noise in configuration space is not homogeneous, the covariance of noise on Fourier wave numbers is correlated. Therefore, we carry out our derivation in configuration space.

Taking a shapelet mode  $M_{nm}$  as an example, the measurement error on the shapelet mode is (Plancherel theorem)

$$\delta M_{nm} = \iint \mathrm{d}^2 x \, (g_{nm}(x))^* \, n_x \,, \tag{D2}$$

where  $g_{nm}(x)$  is the inverse Fourier transform of the shapelet basis function deconvolved by the PSF:

$$g_{nm}(\mathbf{x}) = \left(\frac{1}{2\pi}\right)^2 \iint d^2k \, \frac{(\tilde{\chi}_{nm}(\mathbf{k}))}{p_{\mathbf{k}}} e^{i\mathbf{k}\cdot\mathbf{x}} \,. \tag{D3}$$

The covariance between  $\delta M_{nm}$  and  $\delta M_{n'm'}$  is

$$K_{M_{nm}}^{M_{n'm'}} = \iint d^2x (g_{nm}(\mathbf{x}))^* g_{n'm'}(\mathbf{x}) (f_{\mathbf{x}} + B_{\mathbf{x}}) .$$
 (D4)

The covariances between measurement errors can be estimated in real observations as long as we can estimate  $f_x + B_x$  from single exposure images before subtracting the sky background.

# APPENDIX E: TESTS FOR THE HEAVILY BLENDED CASE

In this appendix, we show the multiplicative bias and additive bias for the blended image simulation introduced in Section 3.3.2 with input galaxy number density of 170 arcmin<sup>-2</sup> (double our fiducial density) in Figures C2 and C3. Similar to the tests in Section 4.2.2, we use two different smoothing scales,  $\sigma_h = 0'.59$  and  $\sigma_h = 0'.45$ , to detect, select and measure shear from the simulated images. These are stress tests of the algorithm under extreme conditions (e.g., near the center of a galaxy cluster).

For each one of the smoothing scales, the result is consistent with the one using the same smoothing scale in Section 4.2.2 at the  $2\sigma$  level